Optimization of Hydrogenated Amorphous Si Layer for Si Heterojunction Solar Cells

Hanchen Liu

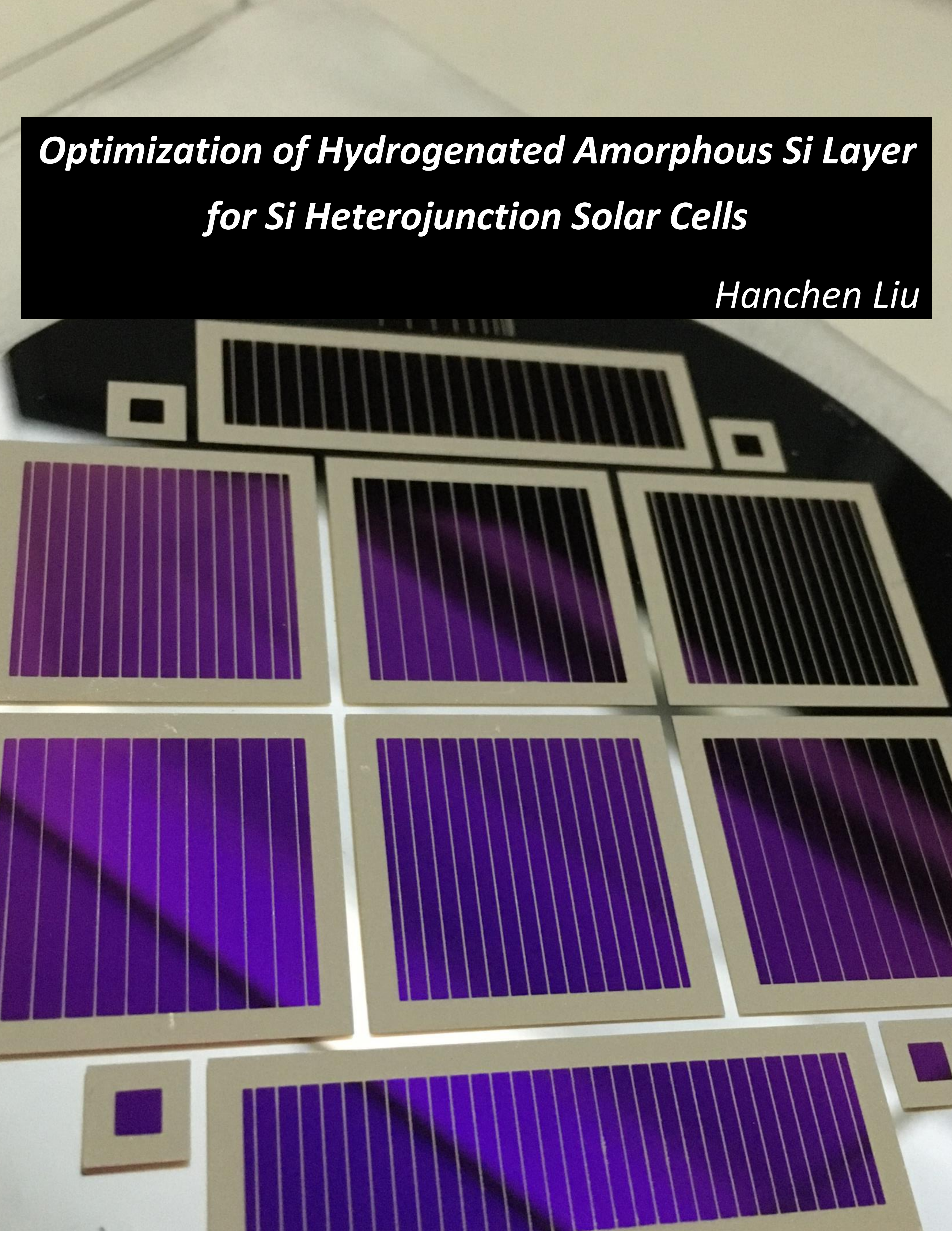

EKL Else Kooi Laboratory

TU Delft Delft University of Technology

PVMD Delft University of Technology

Graduate

Hanche Liu

MSc Sustainable Energy Technology

Faculty of Electrical Engineering, Mathematics of Computer Science (EEMCS)

hanccl96@gmail.com

Supervisor:

Dr. Olindo Isabella, PVMD/ESE

Ir. Yifeng Zhao, PVMD/ESE

MSc Thesis Committee:

Dr. Olindo Isabella, PVMD/ESE

Dr. Rudi Santbergen, PVMD/ESE

Dr. Sten Vollebregt, ECTM

Dr. Luana Mazzarella, PVMD/ESE

Ir. Yifeng Zhao, PVMD/ESE

Delft University of Technology

Department of Electrical Sustainable Energy

Photovoltaic Materials and Devices

ABSTRACT

Crystalline silicon (c-Si) solar cells that are well-established technologies have already achieved a power conversion efficiency (PCE) as high as 26.7% by using the interdigitated-back-contacted (IBC) configuration. However, this efficiency is still limited by the spectral mismatch between the absorption characteristics of c-Si and the AM 1.5 spectrum. To better utilize especially the low wavelength irradiance and to exceed the single-junction silicon solar cell theoretical PCE limit (29.43%), the perovskite/c-Si tandem solar cell concept was proposed.

This thesis project aims to develop a high efficiency single-side textured front-back contacted (FBC) silicon heterojunction (SHJ) solar cell as the bottom cells for 2-terminal (2-T) perovskite/c-Si tandem solar cells. Therefore, we firstly focus on the optimizations of the deposition parameters (power and precursor gases) of hydrogenated intrinsic amorphous silicon ((i)a-Si:H) passivation layer and the subsequent application of hydrogen plasma treatment (HPT) on the (i)a-Si:H layer. An optimized 8.8 nm-thick single (i)a-Si:H together with hydrogen plasma treatment (HPT) achieve an effective lifetime (τ_{eff}) of 1.3 ms, implied open-circuit voltage (iV_{OC}) of 704.3 mV on symmetrical passivated double-side-flat <100> oriented crystalline silicon (c-Si) wafer. To further improve the passivation, a bilayer structure of (i)a-Si:H with a total thickness of 10 nm is optimized to boost further the τ_{eff} to 8.3 ms and iV_{OC} to 733.5 mV.

Afterwards, we implement the optimized (i)a-Si:H layers into the front/back-contacted (FBC) rear junction solar cells with single-side textured morphology, which is designed to be used as the substrate for future integration of solution-processed perovskite top cell. For solar cells investigated, we keep the textured rear side always the same with optimized contact stacks consisting of p-type hydrogenated nanocrystalline silicon oxide ((p)-nc-SiO$_X$:H) and p-type hydrogenated nanocrystalline silicon ((p)-nc-Si:H, while varying the layer stacks on the flat front side. Specifically cell performances are studied with either n-type hydrogenated nanocrystalline silicon ((n)-nc-Si:H) or n-type hydrogenated amorphous silicon ((n)-a-Si:H) with varied optimized (i)a-Si:H layers. We observe enhanced passivation qualities of solar cell precusors when adding the (n)-nc-Si:H/(n)-a-Si:H layer on top of the (i)a-Si:H, which enables the potential for realizing high-efficiency solar cells.

During the fabrication of FBC-SHJ solar cells, we also find that a thinner (i)a-Si:H on the front side is critical to improve the device efficiency thanks to the effective reduction of both parasitic absorption and carrier transport losses. Accordingly the gain in J_{SC} and FF dominate the improvement of PCE. Lastly, we present rear junction FBC-SHJ solar cell with n optimized stack of (n)nc-Si:H and (i)a-Si:H, with V_{OC} of 711 mV, J_{SC} of 34.82 mA/cm^2, FF of 79.64% and PCE of 19.72%. This optimized solar cell is also considered to be ready for its application in tandem device fabrication.

Contents

List of Tables

List of Figures

Chapter 1 INTRODUCTION

1.1 Solar Energy

The global PV market grows spectacularly these years and is now compatible with industrial facilities, buildings, and homes. The Global Solar Photovoltaic capacity has increased from 23.371 (GW) in 2009 to 485.826 (GW) in 2018. The Asia-Pacific region grew to be the largest market of cumulative capacity, which shares 58.1% of global PV capacity in 2018, led by China, India, and Japan [1].

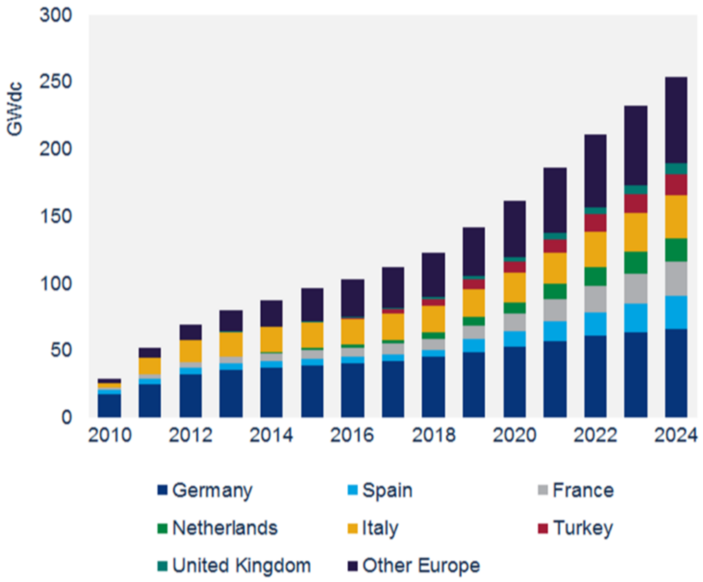

Figure 1.1 The cumulative solar PV installations in Europe from 2010 to 2024. Figure adapted from [2]

For the European market, as shown in Figure 1.1, the cumulative solar PV installations have grown 3 times since 2010. Germany remains the largest PV market and the annual installation in Europe, and the total installed capacity is expected to exceed 250 (GW) by 2024 [2].

1.2 PV Technology

PV has developed for a very long time and it contains many technologies, such as monocrystalline silicon(Mono-Si), multicrystalline silicon(Multi-Si), amorphous silicon(Thin film) and so on. Mono-Si is a high-quality material with almost no defects. High power conversion efficiency can be achieved by using mono-Si and the durability can be more than 25 years. The main disadvantages are the panel's high initial cost and mechanical vulnerability. Compared to mono-Si, multi-Si is cheaper and easier to produce. It assembles multiple grins of silicon crystals into a thin wafer. But because of the grain boundary defects, the power conversion efficiency is not very high. Thin film is depositing Si films onto different substrates, which makes it flexible and much cheaper technology, but the economy sacrifices the power conversion efficiency, and it's sensitive to overheating, which is usually the reason for cell degradation.

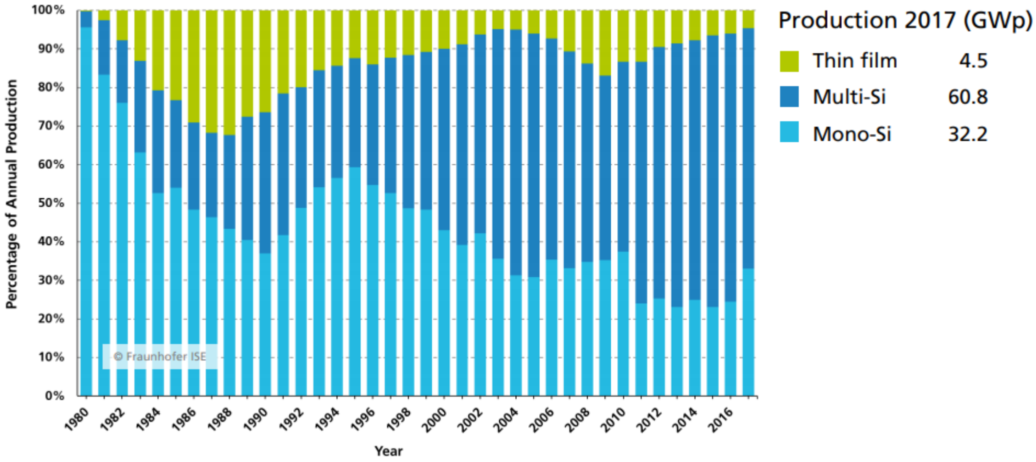

Figure 1.2 Annual production distribution of different PV technologies. Figure adapted from [3]

Figure 1.2 demonstrates the annual production distribution of different technologies. After 2009 the share of silicon wafer keeps increasing and after 2014 silicon wafer has accounted for over 90% in the total production. The segment of multi-Si grows rapidly from less than 5% to over 60% within 40 years.

1.3 High efficiency c-Si solar cell

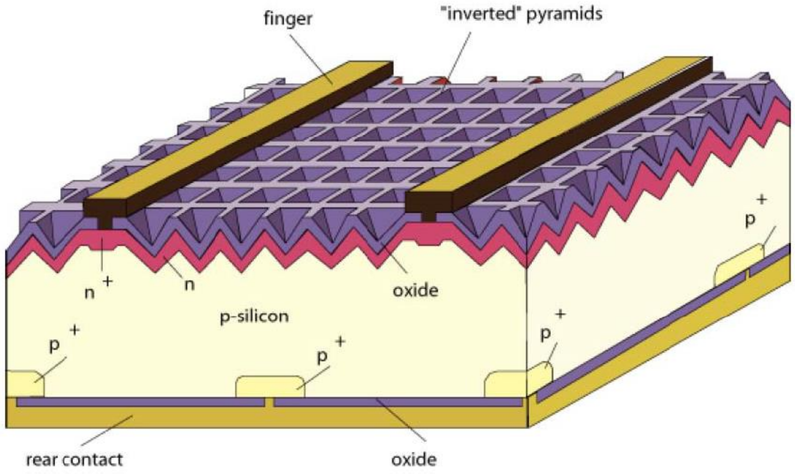

Figure 1.3 The PRRL solar cell structure. Figure adapted from [4]

In the late 1980s and early 1990s, a high efficiency over 25% solar cell was achieved, which is based on crystalline silicon (c-Si) homojunction structure with the concept of PERL (Passivated Emitter with Rear Locally diffused) [5]. As shown in Figure 1.3, the textured surface that features inverted pyramids on the sunny side reduces the surface reflection thus enhancing the total amount of light absorption. Metal contact areas are as small as possible, while the involved silicon regions are locally heavily doped, both together can reduce not only the shading losses and but also the recombination. The surface passivation is made by thermally grown silicon oxide.

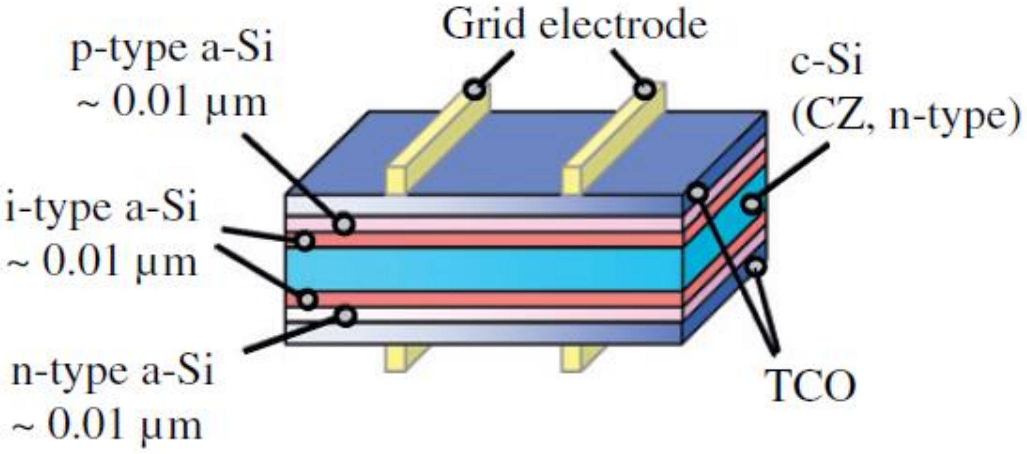

Figure 1.4 The HIT solar cell structure. Figure adapted from [6]

The structure of HIT(Heterojunction with Intrinsic Thin layer) solar cell is illustrated in Figure 1.4. In 1992, SANYO first presented a type of a-Si/c-Si heterojunction solar cell named the HIT solar cell features n-type silicon wafer with p-type amorphous silicon layer ((p)a-Si) on the top as the emitter and n-type amorphous silicon ((n)a-Si) passivation layer on the back forms back surface field (BSF). While between the c-Si and the (n)a-Si, an intrinsic thin amorphous silicon ((i)a-Si) layer is inserted for passivation purposes. The conversion efficiency reached 18.7% for 1 cm^2 cells [7]. In the following years, SANYO continued making progress in HIT solar cells and the certified efficiency with this structure is up to 23% with an area of 100 cm^2 [8].

1.4 Shockley-Quiesser limit

What is the limit of the conversion efficiency of solar cells? Shockley-Queisser limit was raised as the theoretical limit for single-junction solar cells. It contains a spectral mismatch and a detailed balance limit of efficiency.

For spectral mismatch, it assumes that each photon whose energy is higher than the bandgap can generate an electronic charge q. The photons with energy lower than the bandgap are not absorbed and eventually can not generate any charge. So the ultimate conversion efficiency is written as

$$\eta_{ult} = \frac{E_G \int_0^{\lambda_G} \Phi_{ph,\lambda} d\lambda}{\int_0^{\infty} \frac{hc}{\lambda} \Phi_{ph,\lambda} d\lambda} \tag{1-1}$$

Where E_G is the bandgap energy, $\lambda_G = hc/ E_G$ and is the critical wavelength of photons, it corresponds to the photon energy equals to the bandgap energy. $\Phi_{ph,\lambda}$ is the spectral photon flux of the incident light.

For a detailed balance limit of efficiency, it considers both the ambient temperature and solar cell temperature are 300 K. Since the thermal radiation absorption and emission of the cells, the recombination current density will differ from zero and reduce the open-circuit voltage (V_{OC}) and cause efficiency loss.

The efficiency is derived as:

$$\eta = \frac{J_{ph} V_{oc} FF}{P_{in}} \tag{1-2}$$

Where J_{ph} is the photogenerated current density, it equals to the short circuit current density and can be written as

$$J_{ph} = -q \int_0^{\lambda_G} \Phi_{ph,\lambda} \, d\lambda \tag{1-3}$$

P_{in} is the incident solar energy. *FF* is the fill factor.

The bandgap utilization efficiency η_V is defined as the ratio of V_{OC} to the bandgap V_G where $V_G = E_G/q$. And η_V is written as

$$\eta_V = \frac{V_{oc}}{V_G} \tag{1-4}$$

Now by combining (1-5) - (1-6), the efficiency η is given by

$$\eta = \eta_{ult} \eta_V FF \tag{1-7}$$

For V_{OC}, it is calculated by

$$V_{oc} = \frac{k_B T}{q} ln(\frac{J_{ph}}{J_0} + 1) \tag{1-8}$$

where J_0 is the dark current density. We assume the solar cells are under thermal equilibrium at 300 K. For the wavelength shorter than λ_G, the cells absorb and emit thermal radiation as a blackbody. While for the wavelength longer than λ_G the cells are transparent. Based on the blackbody radiation $L_{e\lambda}^{BB}$ we can determine the J_0 as

$$\begin{aligned} J_0(E_G) &= -2q \int_0^{\lambda_G} \int_{2\pi} L_{e\lambda}^{BB}(\lambda; T_a) cos\theta d\,\Omega \, d\lambda \\ &= -2q\pi \int_0^{\lambda_G} \frac{2hc^2}{\lambda^5} [exp(\frac{hc}{\lambda k_B T_a}) - 1]^{-1} d\lambda \end{aligned} \tag{1-9}$$

where θ is the polar angle, $d\Omega$ stands for solid angle element, T_a is the ambient temperature, *h* is Planck constant, *c* is the light speed in a vacuum, k_B is the Boltzman constant. And the factor 2 represents there are 2 emission surface, front and back sides.

FF can also be approximated as a V_{OC} dependent variable below

$$FF = \frac{v_{oc} - ln(v_{oc} + 0.72)}{v_{oc} + 1} \tag{1-10}$$

with $v_{oc} = qV_{oc}/k_B T$.

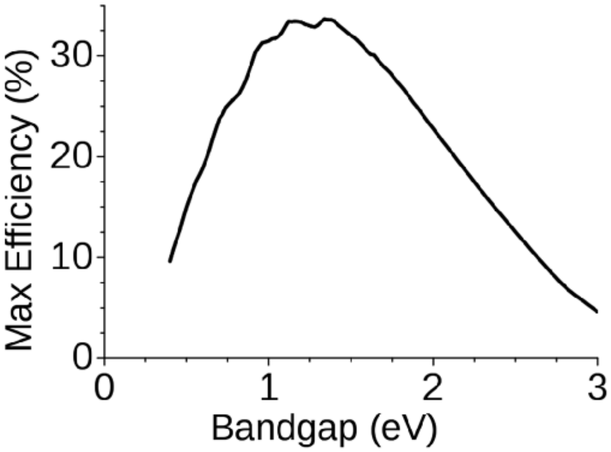

Figure 1.5 Shockley-Quiesser limit efficiency. Figure adapted from [9]

Based on all the derivation above, Figure 1.5 demonstrates the Shockley-Quiesser efficiency limit for the AM1.5 solar spectrum. Two local maximum efficiencies are 33.85% at 1.15 eV and 33.16% at 1.34 eV [10].

1.5 Perovskite/c-Si Tandem Solar Cells

Based on the Shockley-Quiesser limit, under the AM1.5 solar spectrum, c-Si solar cell's efficiency can reach maximally above 30%. But this limit is not directly applicable to c-Si since the dominant recombination mechanism for c-Si is Auger recombination, instead of radiative recombination that used in the derivation above. In 2013, it was published that c-Si solar cell has a theoretical ultimate efficiency of 29.43% under AM1.5 [11].

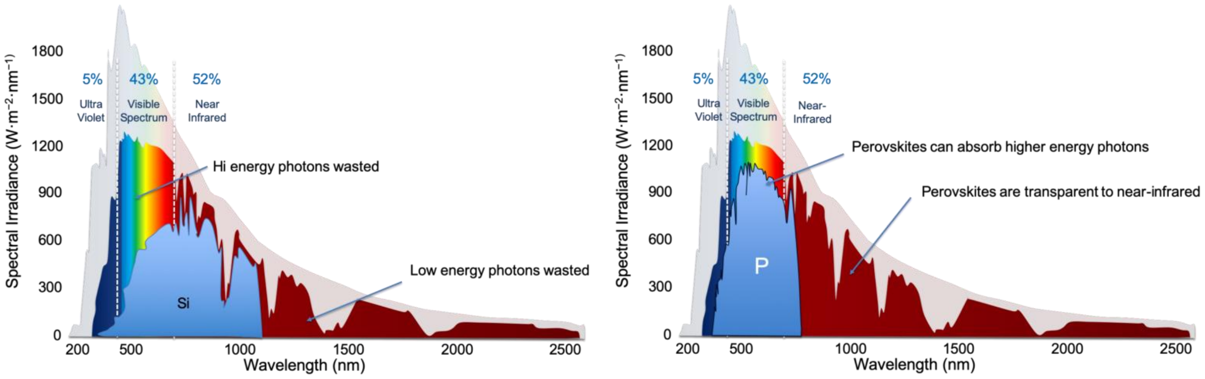

Figure 1.6 (a) spectral irradiance absorption of silicon; (b) spectral irradiance absorption of perovskite. Figure adapted from [12]

Figure 1.6 (a) shows the spectral irradiance and the absorption of silicon. Since the bandgap limitation, much of the ultraviolet irradiance cannot be harvested. But silicon shows a good infrared irradiance response till its bandgap. Figure 1.6 (b) shows the absorption profile of perovskite. Compared to silicon, perovskite match better with AM1.5 spectrum in low wavelength range, in other words, the ultraviolet and visible spectrum are highly effective absorbed till around 780 nm, which corresponds to its bandgap. Beyond 780 nm the absorption drops drastically, making perovskite transparent to infrared spectrum. However, it is not wise to waste the infrared light, which accounts for more than half of the solar energy under AM1.5 spectrum. Therefore, to better utilize spectral irradiance, tandem cells consist of higher bandgap perovskite top cells and lower bandgap silicon bottom cells are proposed [13] [14] [15]. While this also offers flexibility in terms of the tunable bandgap of perovskite top cell in a range of 1.48-2.23 eV. Photons with high energy are mainly absorbed by the top cell while the remaining photons with energy below the bandgap of the perovskite top cell will penetrate through the top cell and reach the bottom cell.

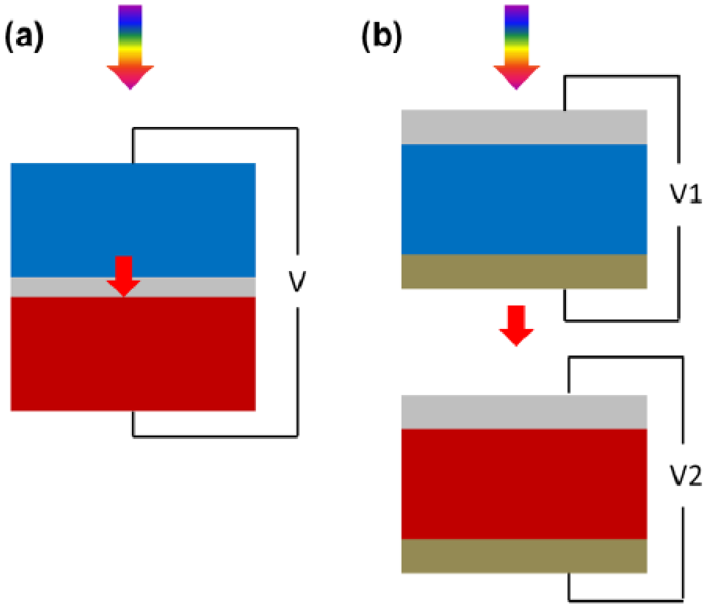

Figure 1.7 The most widely researched tandem structure (a) 2-T; (b) 4-T. Figure adapted from [16]

The classification is based on the electrical topology of the top and bottom cells, the designs of tandem solar cells include mechanically stacked solar cells with 4 terminals (4-T) design [17] just as Figure 1.7 (b) shows, and monolithic electrically connected solar cells which is demonstrated in Figure 1.7 (a). For monolithic tandem solar cells, also referred to as 2-terminals (2-T) architecture [17], the top and bottom cells are series-connected by a tunnel junction [18] [19], thus the current of the tandem solar cells will be constrained by the lower current under maximum power point. Compared to the 4-T, 2-T only requires one semi-transparent electrical contact while 4-T needs at least three semi-transparent contacts to let light into the device. Since there doesn't exist perfectly transparent contacts, the ultimate efficiency for 2-T is higher [19]. This thesis project is to optimize the silicon heterojunction (SHJ) solar cell as the bottom cell in the perovskite tandem application. And the condition to build up the whole device is required at a relatively low temperature (~200 °C) since the bottom silicon solar cell is temperature-sensitive and also needs to be used as the substrate of the top perovskite solar cell.

1.6 Research Goals

To eventually realize the highly-efficient perovskite/c-Si tandem devices, we need to face or overcome some main challenges on the bottom cell. In the 2T perovskite/c-Si tandem solar cell, it is widely accepted that the bottom c-Si cell limits the current output [20] [13], it is required to have a good response to infrared wave. Besides, The most popular way to deposit perovskite solar cells is by spin-coating [21] [22] [23], which requires substrates with flat surfaces.

To address the optical challenges, the rear side textured surface morphology for SHJ solar cells is applied to prolong the infrared absorption [24] [25] [26]. While addressing the process challenge, we choose to have the front side flat for the bottom cell. Considering the flat substrate atom orientation is <100>, the deposited (i)a-Si:H layer needs to be sufficient to saturate the dangling bonds but also avoiding epitaxial growth at c-Si/(i)a-Si:H interface [27] [28].

Besides, because of a more efficient and balanced charge carrier injection of perovskite cell with n-i-p configuration [29], in this study, we mainly investigated the rear junction SHJ cells.

Therefore, the main scientific research goals of this thesis project are:

- Optimize the deposition conditions of (i)a-Si:H on <100> flat c-Si surface to realize both good passivation and high uniformity.
- Fabricate and Optimize the rear junction SHJ solar cells:
  - Investigate different n-doped layers.
  - Optimize the thickness of doped layers

1.7 Outlines

Chapter 1 introduces the background of the PV market, the high-efficiency c-Si solar cells, and also the original intention of why to fabricate these FBC-SHJ solar cells. Chapter 2 introduces the fundamentals of solar cells, including the working principle and the mechanisms of recombination. And emphasizes what is heterojunction solar cell from the band diagram and the transport mechanism. Chapter 3 talks about how to fabricate a solar cell including the cleaning process and the later measurement, the tools used in characteristic measurement are also investigated. The optimization of passivation by (i)a-Si:H is presented in chapter 4. It contains the determination of various parameters during deposition and also the post-treatments. After the passivation layer, the process of fabricating a solar cell device is recorded in chapter 5. The manufacture of FBC solar cells requires the optimized doped layer in terms of both types and thickness, which has a direct impact on FF, J_{SC}, and V_{OC} [30] [31] [32].

Chapter 2 FUNDAMENTAL

2.1 Working Principle of Solar Cell

The working principle of solar cells is based on photovoltaic effect, i.e. a junction of two different materials will generate a potential difference in response to the incident electromagnetic radiation, commonly the solar radiation. Albert Einstein explained the wave-particle duality of light and assume the existence of the particulate quality energy quanta as photons. The energy of the photon is expressed as:

$$E = h\upsilon \tag{2-1}$$

where h is the Planck's constant and v is the light frequency. When the light incidents into the absorber, only the photons that have higher energy than E_G can excite the electrons boost into the conduction band and leave the holes in the valence band. E_G is the energy difference of the conduction band edge (E_C) and valence band edge (E_V).

The generated charge carriers need to be separated by semipermeable membranes, which usually formed by the p- and n-type materials and then transport to the external circuit to realize the utilization of solar energy.

2.2 Semiconductor Materials

Nowadays c-Si solar cell is still the most extensively used material in the photovoltaic market because of its suitable bandgap, high energy efficiency, cost competitiveness, good stability, and non-toxicity [33].

Per Si atom has 4 valence electrons, since two electrons can form the so-called covalent bond, a Si atom can bond with 4 other neighboring atoms and share the electrons as Figure 2.1 shows. The lattice unit cell of crystal Si is a face-centered cubic with 4 inner atoms, which are at the diagonal direction, near the corner atom. And Si can either gain 4 extra electrons or lose 4 electrons to be stable.

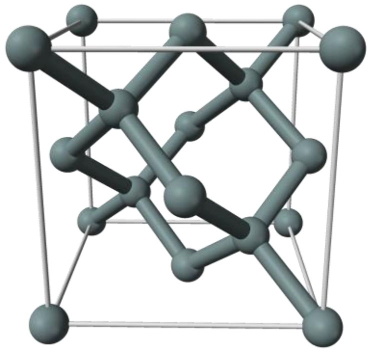

Figure 2.1 Unit cell of crystal silicon. Figure adapted from [34]

Amorphous silicon (a-Si) is a direct bandgap semiconductor material, the bandgap is in the order of 1.6 to 1.8 eV. Compared to c-Si, a-Si is a defect-rich material. Figure 2.2 shows the 2D structure of c-Si and a-Si, the c-Si is highly regulated and long-range ordered, which has fewer defects inside, while the amorphous is more like a “none range ordered” random continuous network formed by silicon atoms, and the defect density is extremely high.

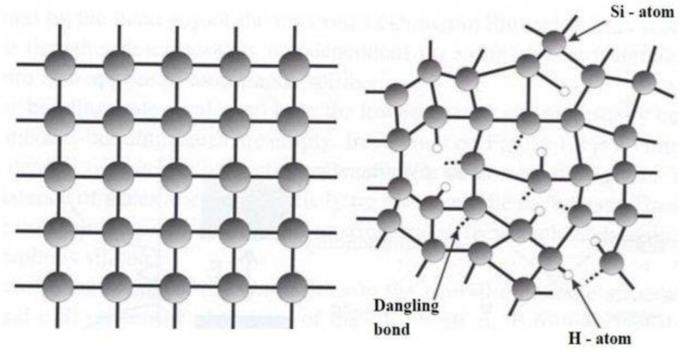

Figure 2.2 Schematics of crystalline silicon and amorphous silicon. Figure adapted from [35]

2.3 Recombination Mechanism

2.3.1 Radiative recombination

It is the reverse process of the photogeneration. The excited electron falls back to the equilibrium band and recombines with a hole, the energy is emitted as a photon. This mechanism plays a major role in the direct bandgap semiconductor [36].

2.3.2 Auger recombination

Auger recombination is regarded as a three-particles process. The energy that comes from the electron-hole pair recombinations will be given to the third carrier, either an electron or a hole. Then this third electron or hole is excited into a higher energy level of conduction band or valence band, respectively. This additional energy will be transferred into the lattice vibration energy because of the collision, and the carrier will be relaxing back to the band edge and dissipate energy as heat [37].

2.3.3 Shockley-Read-Hall(SRH) recombination

SRH recombination is facilitated by impurities or lattice defects. Within the forbidden gap, there will form allowed energy states called trap states, which play the role of recombination center, i.e. a conduction electron can be trapped into the trap states and relax to the valence band, annihilating with a hole [36] [37].

2.3.4 Surface recombination

Since the crystal silicon lattice has an abrupt ending at the surface, the defects and impurities at the surface will lead to promoting recombination.

For heterojunction silicon solar cell, we use c-Si as substrate and put thin-film Si layer above, which require a higher bandgap and also good passivation. Usually, we use a-Si:H as the layer, since it has less grain boundary defects and easy to deposit.

The carriers effective lifetime τ_{eff} is calculated by the equation below

$$\frac{1}{\tau_{eff}} = \frac{1}{\tau_{rad}} + \frac{1}{\tau_A} + \frac{1}{\tau_{SRH}} + \frac{1}{\tau_S}$$

$$= \frac{1}{\tau_{bulk}} + \frac{1}{\tau_S} \qquad (2\text{-}2)$$

Where the τ_{rad} is the radiative lifetime, τ_A is the Auger lifetime and τ_{SRH} is the SRH lifetime. These three components form the material bulk lifetime τ_{bulk}. τ_S is the surface lifetime. For indirect bandgap material such as c-Si, τ_{rad} is very small that could be neglected. τ_{SRH} is related to the level of the defect and τ_A is related to the excess carrier concentration. If the wafer itself is high-quality and contamination-free, the τ_{bulk} can be ignored when compared to the τ_S. Generally, either for stacking layers or solar cells, surface recombination domains the effective lifetime.

τ_S can be written as

$$\tau_S = \frac{W}{2*S} \qquad (2\text{-}3)$$

where the W means the wafer thickness and S is the surface recombination velocity. Surface recombination velocity is given by

$$S = \vartheta_{th}\sigma N_{ST} \qquad (2\text{-}4)$$

it is the production of these three parameters, where v_{th} is the thermal velocity (cm/s), σ is the capture cross-section for minority carrier (cm^2), and N_{ST} is the surface trap density (cm^{-2}). Under a fixed temperature, there are two ways to improve the carrier lifetime:

1. reduce the minority carrier concentration on the interface
2. decrease the surface trap density

To achieve these two goals requiring field-effect passivation and chemical passivation, respectively.

2.4 Heterojunction Solar Cells

With the increased demand for energy, solar energy as a prominent source attracts most focus, people are upgrading the solar cell by researching the combination of different materials and optimizing the processing steps. The silicon heterojunction solar cell is one of the products. It can grow the a-Si layer at a very low temperature, e.g., as low as 30°C [38]. As for annealing, silicon heterojunction solar cell doesn't need very high temperature, which lowers the temperature budget [39].

2.4.1 Band structure

Heterojunction can be described as the interface between the two materials that have different semiconductor properties, such as energy bandgaps [4] [40].

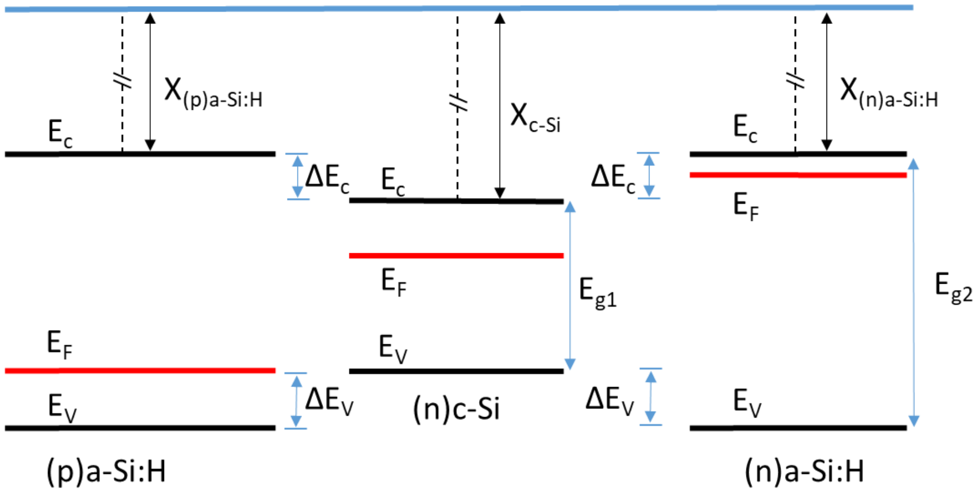

Figure 2.3 Energy band diagram of p-doped a-Si:H layer, n-doped c-Si and n⁺-doped a-Si:H layer

Figure 2.3 shows the way how to form the heterojunction. The n-type c-Si has a bandgap of 1.1 eV, while the doped a-Si:H has a bandgap of 1.7 eV. The electron affinity of c-Si is $\chi_{c-Si} = 4.05\ eV$, while for a-Si:H is $\chi_{a-Si:H} = 3.93\ eV$ [41].

In Figure 2.3 the vacuum layer is aligned and there is an energy difference between bandgap. The ΔE_C and ΔE_V represent the band offset within the conduction and valence band. They can be presented with related parameters as

$$\Delta E_C = \chi_{c-Si} - \chi_{a-Si:H} \tag{2-5}$$

$$\Delta E_V = (E_{Ga} + \chi_{a-Si:H}) - (E_{Gc} + \chi_{c-Si}) = \Delta E_G - \Delta E_C \tag{2-6}$$

Where E_{Ga} and E_{Gc} is the bandgap of a-Si:H and c-Si, respectively.

The Quasi-Fermi energy describes the conduction (valence) band state occupation of electrons (holes) under non-equilibrium. The energy difference between conduction (valence) band and the quasi-Fermi level in n(p)-type a-Si:H is shown by

$$E_C - E_{Fn} = k_B T ln(\frac{N_C}{n}) \tag{2-7}$$

$$E_{Fp} - E_V = k_B T ln(\frac{N_A}{p}) \tag{2-8}$$

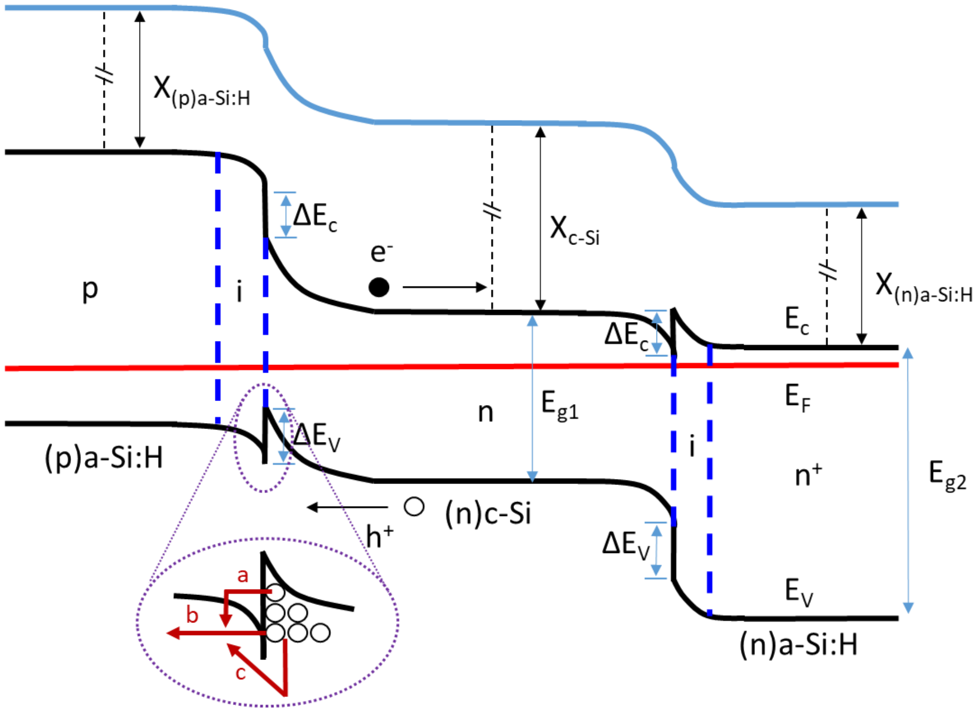

Figure 2.4 The band diagram of n-type SHJ solar cells under dark and thermal equilibrium. The carrier transport direction and mechanisms are shown, where (a) is trap-assisted tunnelling (TAT) [42] [43]*, (b) is direct tunnelling (DT)* [44] [45] *, and (c) is thermionic emission (TE)* [45]

When "connect" the materials, the band diagram is shown in Figure 2.4, the Fermi energy is aligned and constant through the whole junction while under equilibrium. And in the band bending, the same offsets ΔE_C and ΔE_V will exist at the interface, which is known as the electron affinity rule. There will form a transport barrier at the interface, which can suppress the majority carrier i.e. electrons transport from c-Si to the p-type a-Si:H. Meanwhile, there will be a narrow "spike" barrier for holes, which can drift through by direct tunneling, trap-assist tunneling, and thermionic emission.

In summary, the advantages of heterojunction solar cells are less carrier recombination at the junction interface, which can gain a higher photocurrent.

2.4.2 Doped layer

The doped layer is grown by adding the doping atom, phosphorus for n-type, and boron for p-type, into precursor gas. The doping level depends on the concentration of doping impurities. A higher concentration of doping impurities leads to lower activation energy (E_a). There are usually two types of doped layer, a-Si:H or nc-Si:H. Compared to a-Si:H layer, the doping efficiency is higher on nc-Si:H since the doping impurities prefer at the crystalline phase, so the conductivity of doped-nc:Si:H increases up to several orders of magnitude. The doped layer is very important since it can affect V_{OC}, J_{SC}, FF, and contact resistance [30] [31] [32].

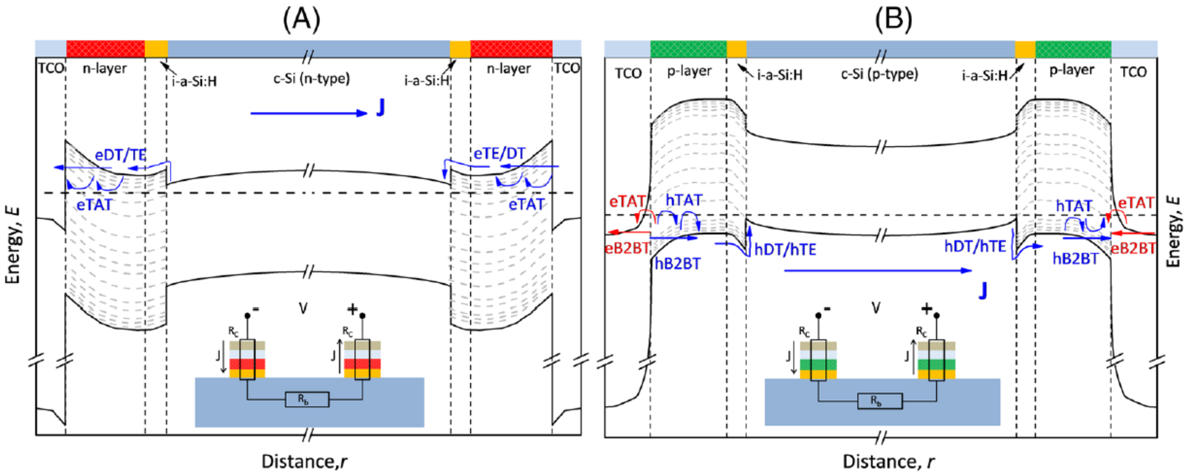

Figure 2.5 Band diagram of transfer length method for (a) n-type layer and (b) p-type layer. The majority charge carriers' transport mechanisms are illustrated. For n-type layer, electrons can transport by TAT, TE and DT through conduction band; as for p-type layer, the transport mechanisms from the valence band to TCO contains also band-to-band tunnelling (B2BT). Figure adapted from [32].

Figure 2.5 shows the band diagram of (a) n-type layer and (b) p-type layer. The transport of charge carriers in the n-doped layer includes DE, TE, and TAT. As for the p-doped layer, the transport mechanism of holes includes DT, TE, TAT, and band-to-band tunneling (B2B) at the interface of the p-doped layer/TCO.

For n-contact, low activation energy (E_a) is required for good carrier transport since:

I. Low E_a can enhance band bending at the c-Si/(i)a-Si:H interface [32];
II. Low E_a can reduce the energy barrier for electrons transport, and thus the probability for tunneling is higher.

For p-contact, a wilder E_g of p-type layer can improve the c-Si interface band bending [46]. Generally, the E_g of (p)nc-Si:H and (p)a-Si:H is around 1.1 and 1.7 eV, respectively [47]. To further increase the doped layer bandgap, SiO_X:H and SiC_X:H are induced, their E_g are 1.7-2.2 eV [48] [49] [50] and 1.4-2.1 eV [51] [52], respectively. Also, the nc-SiO_X is a good material as a carrier selective layer with promising optoelectrical properties [53], it would be interesting to develop a doped layer which is compatible with nc-SiO_X.

And the carrier transport from p-type layer to TCO relies on B2B and TAT mechanism, which is more complex. The B2B is a more efficient way compared to TAT since the holes will directly jump to the conduction band of TCO and recombine with electrons, which functionally lead to current flow [32].

To increase the V_{OC}, the recombination should be suppressed. At c-Si/(i)a-Si:H interface, the recombination is related to the defect density and carrier concentration [54]. A huge difference between the majority and minority carriers can reduce the recombination rate and make it less sensitive to dangling bonds density. This can be achieved by a strong band bending at the c-Si interface, which can increase the energy states of holes, and thus, the Fermi level is getting close to the valence band and the E_a is low [46].

2.4.3 The growth of nc-Si:H

The growth of nc-Si:H is shown in Figure 2.6, it is a transition from a-Si:H layer to a layer with high crystalline volume fraction (F_C). The incubation layer is an amorphous layer, which starts to have nucleus formation. After that, the “seed” grows into nanocrystal and go through stationary growth. Nanocrystalline growth involves several factors such as deposition parameters [55], substrate selectivity [56], the thickness of the film [57], and the doping gas [58].

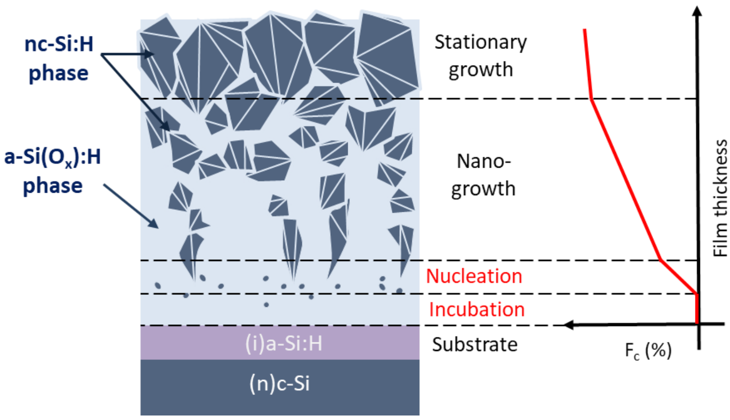

Figure 2.6 The growth of nanocrystalline silicon based on an (i)a-Si:H [59][57]. *The crystalline volume fraction F_C is a function of film thickness. Figure adapted from* [60].

Chapter 3 EXPERIMENTAL METHODS

3.1 Processing Methods

This section talks about the solar cell fabrication process from a n-type double-side-polished <100> c-Si wafer. Firstly, the wafer will be processed to a single side textured wafer, then it will go through the wet-chemical cleaning, and followed by Plasma Enhanced Chemical Vapour Deposition (PECVD) to deposit Si thin film layers on the wafer substrate. Then magnetron sputtering is used to deposit TCO layers on both sides and finally screen printing is for forming metal contacts.

3.1.1 Wafer texturing

To get a single-side textured wafer, firstly a silicon nitride (SiN_X) layer grows on one side of the polished wafer by PECVD. This SiN_X layer is used as an etching resistant layer, which protects the polished surface from being textured. Then <100> c-Si is etched by 5% tetramethylammonium hydroxide (TMAH) at 80°C for 10 minutes, the non-protected side will be etched to form random pyramids. Later, the wafer is immersed in 0.55% HF for approximately 15 minutes to remove the silicon nitride layer.

3.1.2 Wet-chemical cleaning

Wet chemical steps aim to prepare a smooth, non-contaminated surface for the subsequent processing. This cleaning line contains three steps:

- Immerse wafer in 99% room-temperature HNO_3 for 10 minutes.
- Immerse wafer in 69.5%, 110°C HNO_3 for 10 minutes.
- Immerse wafer in 0.55% HF for 5 minutes to remove the native oxide that is formed on the wafer surface and the wafer surfaces become hydrophobic.

3.1.3 Plasma Enhanced Chemical Vapour Deposition (PECVD)

PECVD is a glow charge chemical vapor deposition, using plasma as activation energy instead of thermal energy so that the deposition can carry through under relative-low temperature.

After the wet-chemical cleaning, the wafer will be put into a holder transferred into the deposition chamber as soon as possible to avoid surface oxidation. Multi-chambers are classified for different doping of the thin-film layers. shown in Figure 3.1.

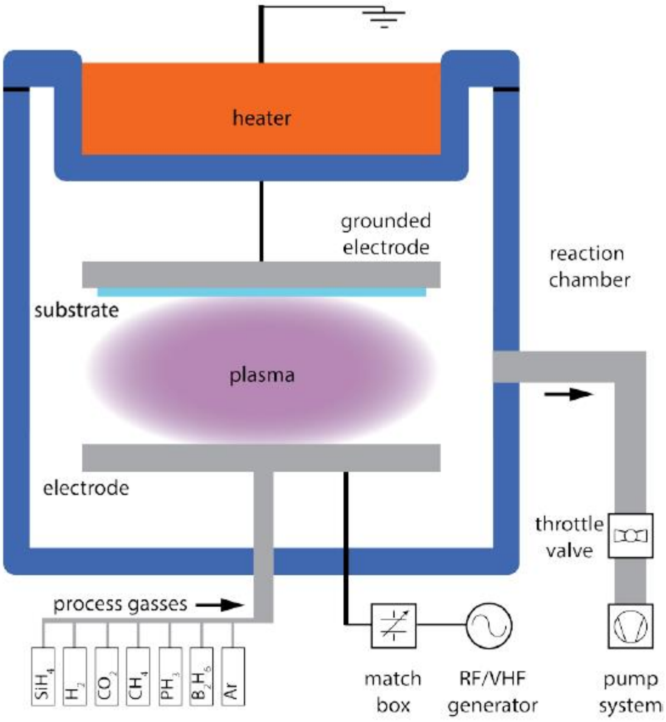

Figure 3.1 Schematic diagram of PECVD setup. Figure adapted from [61]

The general operation steps are:

- Condition chamber and holder for achieving rather controllable initial condition for thin-film depositions.
- Preheat wafer for 40 minutes.
- Purge the chamber for 2 minutes.
- Set the precursor gas flow and chamber pressure, wait for 5 minutes till both the gas flows and the pressure are stable.
- Turn on the Radio Frequency power, set the load/tune position automatically or manually.
- Ignite the plasma.

Within the highly energetic plasma, the precursor gases will be ionized and dissociated into active radicals by collision with electrons. The active radicals will diffuse near the substrate surface and sustain a heterogeneous chemical reaction and grow the thin film layer.

The involved PECVD equipment includes AMOR and AMIGO. Amor is manually operated and AMIGO can be automatically operated with a certain recipe. Both of them feature parallel-plate discharge electrodes with showerhead gas inlet for improving the deposition uniformity.

3.1.4 Radio-Frequency Magnetron Sputtering

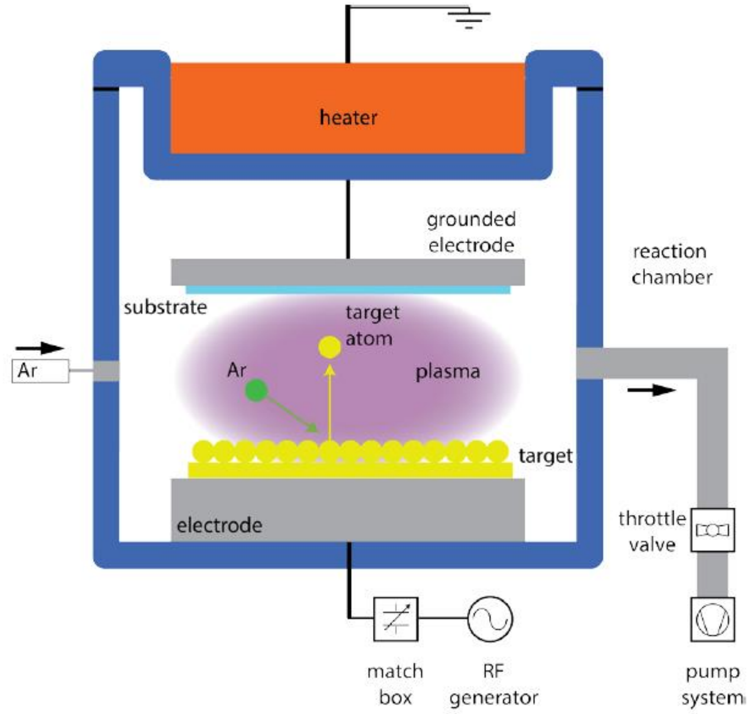

Figure 3.2 Schematic configuration of the sputtering process. Figure adapted from [61]

Sputtering is a widely used thin film deposition technique, which is a non-thermal vaporization process. Sputtering uses glow discharge to generate a flux of accelerate ionized atoms that incident on the surface of the target and eject atoms from the solid target. The ejected atoms will be accumulated on the sample surface and nucleate to form a thin film layer. The process is shown in Figure 3.2.

To sputter the insulating materials, instead of DC power, an alternating radio-frequency(RF) source is chosen. Generally, RF supplies electrodes 13.56 MHz or some multiple. For magnetron sputtering, usually, permanent magnets are used to produce strong magnetic fields, which can confine the secondary electrons near the target surface environs. Thus longer electrons residence time will be achieved and result in better sputter atoms ionization, denser plasma, and a higher deposition rate [62].

3.1.5 Screen Printing

Screen printing is the process of transferring paste through the apertures to be deposited on the substrate in a mannered way. It is realized by a flexible squeegee stroking the paste across the screen surface. In this study, the paste is a silver-based polymer and the general material for mesh is polyester. The sample is placed on the working desktop first and the position is aligned, the sample attaches bottom by vacuum. Then the substrate moves under the screen and lifts. The squeegee will press down the mesh, which will tightly form a line contact with the sample. Then the squeegee will travel across the substrate while pushing the paste to penetrate the aperture to form Ag contacts [63]. After that, the samples are annealing into 170 °C for 30 minutes.

3.2 Characterization Methods

This section introduces the characterization methods for thin-film layers and solar cells.

3.2.1 Minority-carrier lifetime

Minority-carrier lifetime is important since a higher lifetime means the higher possibility that carrier can be collected as current in the solar cell. The lifetime tester (Sinton WCT-120) uses the Eddy-current method. A coil incorporated sensor is near the wafer sample and emits electromagnetic waves into the light, which is then pulsed on the wafer surface to create excess carriers. Due to the excess carriers, the conductance will increase and be detected by the sensor.

The way to analyze the data is by using transient photoconductance techniques and the Quasi-steady-state Photoconductance (QSSPC) method. For examples, light incident into a p-type semiconductor, the continuity equation for free carrier generation without surface recombination is

$$\frac{\partial \Delta n(t)}{\partial t} = G - R = G - \frac{\Delta n(t)}{\tau_{eff}} \tag{3-1}$$

Where the $\Delta n(t)$ is the excess minority carrier concentration, G is the generation rate while R is the recombination rate, τ_{eff} is the effective lifetime. Solving the equation above we can get

$$\tau_{eff} = \frac{\Delta n(t)}{G(t) - \frac{d\Delta n(t)}{dt}} \tag{3-2}$$

This is the generalized data for quasi-transient and quasi-steady-state measurements. In transient photoconductance decay, where $G(t) \ll \frac{d\Delta n(t)}{dt}$

$$\tau_{eff} = -\frac{\Delta n(t)}{\frac{d\Delta n(t)}{dt}} \tag{3-3}$$

In steady-state photoconductance, where $G(t) \gg \frac{d\Delta n(t)}{dt}$

$$\tau_{eff} = \frac{\Delta n}{G} \tag{3-4}$$

The photo generalization is based on a flashlight with a decay time around several seconds. Due to the high decay time, the sample with a lower effective carrier lifetime(less than the flash lamp time constant)under this mode is quasi-steady-state. The absorption of semiconductor bulk is determined on the reflectivity of the front, back surfaces, and the thickness of the wafer. Generally, the absorption fraction(f) for polished bare silicon wafer is around 0.6, the optimized anti-reflection coating will increase f to around 0.9, while for textured wafer f=1.The generation rate G can be expressed as

$$G = \frac{f\Phi}{d} \tag{3-5}$$

where Φ is the photon flux density and d is the wafer thickness.

Assuming the generation rate is exponentially decay in time, written as

$$G(t) = \begin{cases} 0, & t \leq 0 \\ G_0\, exp\left(\frac{-t}{\tau_{flash}}\right), & t > 0 \end{cases} \tag{3-6}$$

And assume the boundary condition for $\Delta n(0) = 0$, solve the differential equation to calculate $\Delta n(t)$ is

$$\Delta n(t) = \frac{\tau_{flash}\tau_{eff}}{\tau_{flash}-\tau_{eff}} G_0[exp\left(\frac{-t}{\tau_{flash}}\right) - exp\left(\frac{-t}{\tau_{eff}}\right)] \tag{3-7}$$

Since the lifetime is carrier density-dependent, for a single-point measurement, usually $\Delta n = 10^{15} cm^{-3}$ is recommended, which is related to the solar efficiency, a good signal for instruments and good measurements of emitter saturation current density.

3.2.2 Spectroscopic ellipsometry

Ellipsometry is used to as a contact-free tool to measure film thickness and optical properties. It can measure the change in polarization as incident radiation transmitted or reflected with the aim material, which written as

$$\rho = tan(\Psi)e^{i\Delta} \tag{3-8}$$

Where ρ is the change in polarization, Ψ and Δ are the relative amplitude ratio and phase difference between p- and s-polarization. As we know light can be regarded as the electromagnetic waves, the electric field is orthogonal to the propagation direction. The polarized light that has added electric field, which has a unique path and can be distinguished specifically for any point can be regarded as polarized light. Based on their phase and amplitude, the light could be linearly, circularly, or elliptically polarized.

The set up includes a light source, a polarization generator, the measured sample, a polarization analyzer, and a detector. The unpolarized light from the light source will go through the polarization generator, which will allow the preferred electric field orientation pass and become a linearly polarized light. Then the reflected light from the sample will become elliptically polarized and go through the analyzer.

Data analysis is based on the constructed model. Use the Cody-Lorentz model to iterate the generated response and compare the results to the experimental values. The best value corresponds to the global minimum Mean Squared Error (MSE).

3.2.3 Fourier-transform infrared spectroscopy (FTIR)

In infrared spectroscopy, radiation incidents into the sample. Some of the infrared radiation is absorbed by the sample, while others could be transmitted or reflected. Analysis of the resulting spectrum could determine the material because a certain molecular has its unique infrared response.

The process is as follows: firstly, the beam source can generate the infrared energy, which passes through an aperture that controls the incident energy. Then the beam enters the interferometer, the exiting interferogram signal will continue passing through the sample. A detector is then measuring the transmitted interferogram signal, which is sent to the computer to do the Fourier transformation. Finally, a spectrum is presented related to wavenumber. Wavenumber of absorption peaks represents the vibration frequency of bonds that comprise this material, the size of the peaks corresponds to the number of components.

To avoid the background absorption effect and only measure the thin film layer characteristics, we also measure pure silicon wafer substrate since the absorption intensity is a relative value. Thus the presented spectrum can be regarded as thin-film layer character measurement.

3.2.4 The external quantum efficiency (EQE)

The EQE is the portion of incident photons that successfully create electron-hole pairs, which are then collected and transport to the external circuit. It is a wavelength-dependent parameter since it interacts with the bandgap. The measurement is accomplished by illuminating discrete monochromatic light and collecting the photocurrent through the cell. The EQE is derived below:

$$EQE(\lambda) = \frac{I_{ph}(\lambda)}{q\Psi_{ph,\lambda}} \tag{3-9}$$

Where $I_{ph}(\lambda)$ is the photocurrent, q is the elementary charge and $\Psi_{ph,\lambda}$ is the incident photon flow at wavelength λ. And the fraction losses could be blamed on parasitic absorption and penetration length.

Parasitic absorption, which means the light has been absorbed before arriving the absorber by other layers, e.g., (i)/doped a-Si:H layers, but the generated electron-hole pairs within these defect-rich layers can’t contribute to the current output.

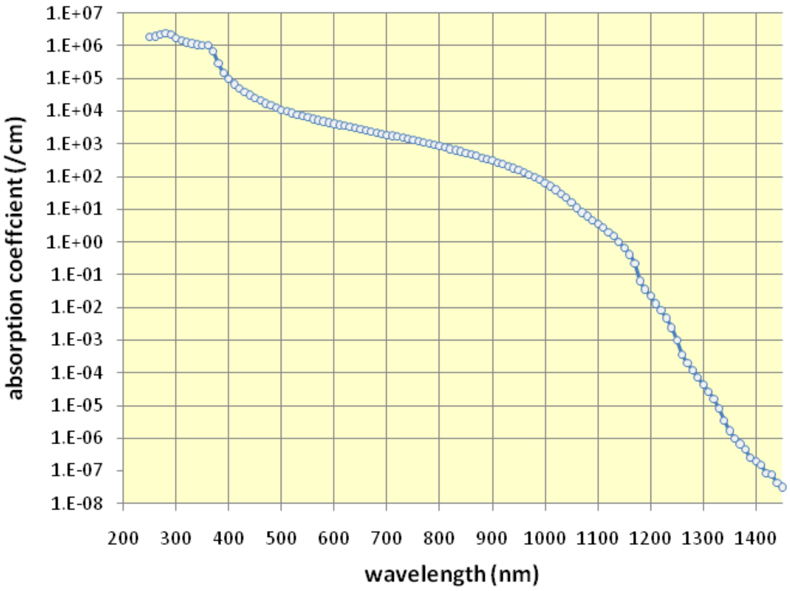

Figure 3.3 Absorption coefficient of Silicon [64] [65]. *Figure adapted from* [66]

Penetration length δ_p is defined as $1/\alpha$ where α is the absorption coefficient. This is derived from Lamber-Beer law

$$I(x) = I_0 exp(-\alpha x) \tag{3-10}$$

where $I(x)$ is the intensity for depth at x, I_0 is the initial intensity. δ_p represents the left intensity is only $1/e$ of the initial value. Figure 3.3 shows the absorption coefficient of c-Si. The wafer thickness in our experiment is around 280 µm, we assume it is the absorption path length and we require the wafer to absorb 90% of the light. Based on the equation $I(x) = I_0 exp(-\alpha x)$ (3-10) we get the satisfied wavelength is around 1080 nm. Longer wavelength requires a longer path length to be absorbed to the same level.

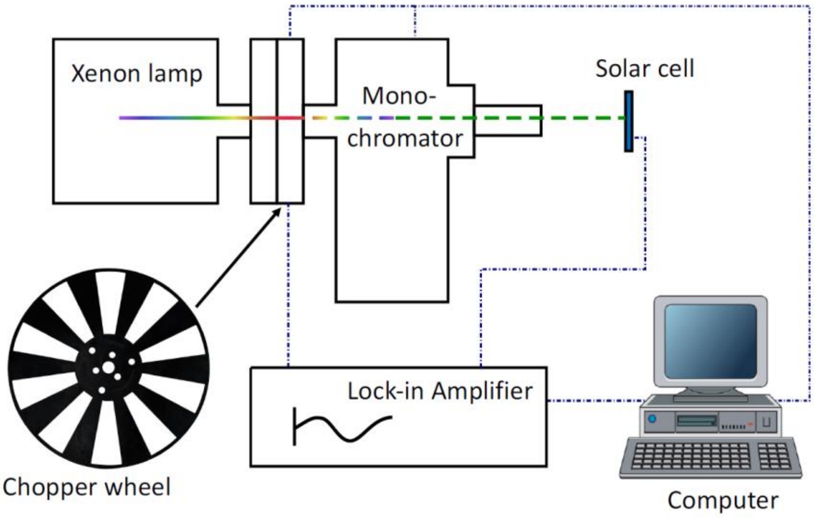

Figure 3.4 EQE measurement setup

Figure 3.4 shows the measurement setup, it includes the light source with a continuous spectrum, a chopper frequency generator, the filters, the monochromator, the lens system, a lock-in amplifier, and a computer. Before measuring the cell, we connect a calibrated solar cell and placed it under the light beam. The filter and monochromator can select a very narrow wavelength range of photons from the light source starting from UV light up to deep infrared. After the calibration, the spectral photon flux is saved in a data file. Then we replace the cell under the beam, it will produce an alternating current signal with low amplitude. This current will pass through the shunt resistor and convert to a voltage drop. Lock-in amplifier is used to remove the noise of the solar cell's response to the monochromator. The signal of the chopper will be a reference signal in the lock-in amplifier, and by using Phase Sensitive Detection (PSD) and low-pass filter, we can get a DC signal that is proportional to the amplitude of the measurement signal. To calculate the EQE of the cell we use the equation

$$EQE(\lambda) = EQE^{ref}(\lambda) \frac{I_{ph}(\lambda)}{I_{ph}^{ref}(\lambda)} \tag{3-11}$$

Under the same spectral condition, EQE is proportional to the photon current, which is the output of the lock-in amplifier, the aim cell's EQE can be determined by the previous calibrate solar cell's measurements. And the $J_{SC,EQE}$ is the $I_{ph}(\lambda)$ integral over wavelength from 300 nm to 1200 nm.

Chapter 4 OPTIMIZATION OF INTRINSIC LAYER

In this chapter, we conduct optimizations of (i)a-Si:H layer by varying the PECVD deposition parameters and then evaluate the surface passivation quality of (i)a-Si:H passivated n-type FZ <100> flat wafer. Besides, homogeneous distribution of the deposited (i)a-Si:H is also considered as an important measure for further guaranteeing better controls of its application in the solar cells.

4.1 Preliminary processing of the wafer

We use Topsil n-type FZ c-Si <100> double-side polished wafers, which feature resistivity of 1-5 Ωcm and thickness of 280±20 μm. To remove possible contamination before (i)a-Si:H layer deposition, the previously introduced wet-chemical cleaning is required. Wafers immersed in 99% HNO_3 and 69% HNO_3 at ambient temperature for the 10 minutes can remove organic materials and possible metal particles, respectively. After cleaning steps, the wafers are rinsed in the Quick Dump Rinser with the standard program until the resistivity reaches 5 MΩ. Then the wafers are dried by using the "Averager Ultra-Pure 6" dryer with the standard program. The last step is using wet bench 0.55% HF at ambient temperature for 5 minutes to remove oxides.

When the wafers are settled in the deposition chamber, there is a preheating process. Wafers are warmed up for 40 minutes to 180 °C before the deposition starts. The effect of temperature is important since it directly affects the hydrogen content of (i)a-Si:H layer [67]. Based on Koch's research [68] that lower substrate temperature can increase the hydrogen content of (i)a-Si:H layer, but the increase demonstrates a Si-H_2 bonding dominated rise compared to Si-H bonding, bringing a void-rich a-Si:H network, deteriorating the film quality and degrading the passivation.

4.2 Single (i)a-Si:H layer passivation

In this section, we investigate the effects of the PECVD deposition parameters for single (i)a-Si:H layer passivation. Based on the previous work on optimizations of (i)a-Si:H for textured c-Si [69], we choose to firstly investigate the effects of hydrogen dilution ratio and power for (i)a-Si:H depositions. Then, we also study the effects of power and duration of subsequent hydrogen plasma treatment (HPT) [70] on as-deposited (i)a-Si:H layer.

4.2.1 Effect of Dilution Ratio

In this section, the variable Dilution Ratio (DR) is investigated. DR is defined as:

$$DR = \frac{Flow\ rate\ (H_2)}{Flow\ rate\ (SiH_4)} \qquad (4\text{-}1)$$

DR reflects the quantity of H_2 that is involved in the growth of a-Si:H film. Table 4.1 lists the PECVD deposition parameters of (i)a-Si:H during the optimization of DR. The flow rate represents the total flow of the precursor gases (SiH_4 and H_2).

Table 4.1 PECVD deposition parameters of (i)a-Si:H with varied DR

Layers	Substrate Temperature (°C)	Pressure (mbar)	Flow rate (sccm)	Frequency (MHz)	Power (W)	Dilution Ratio (-)
(i)a-Si:H	180	1.4	40	13.56	3	***0-3***

Figure 4.1 shows the thickness measured points on one side of a half wafer. Since in (i)a-Si:H optimization the front and back side are symmetrical deposition, the thickness plots are the average value of 8 points on a half wafer. And the error bar of thickness is derived from the standard deviation.

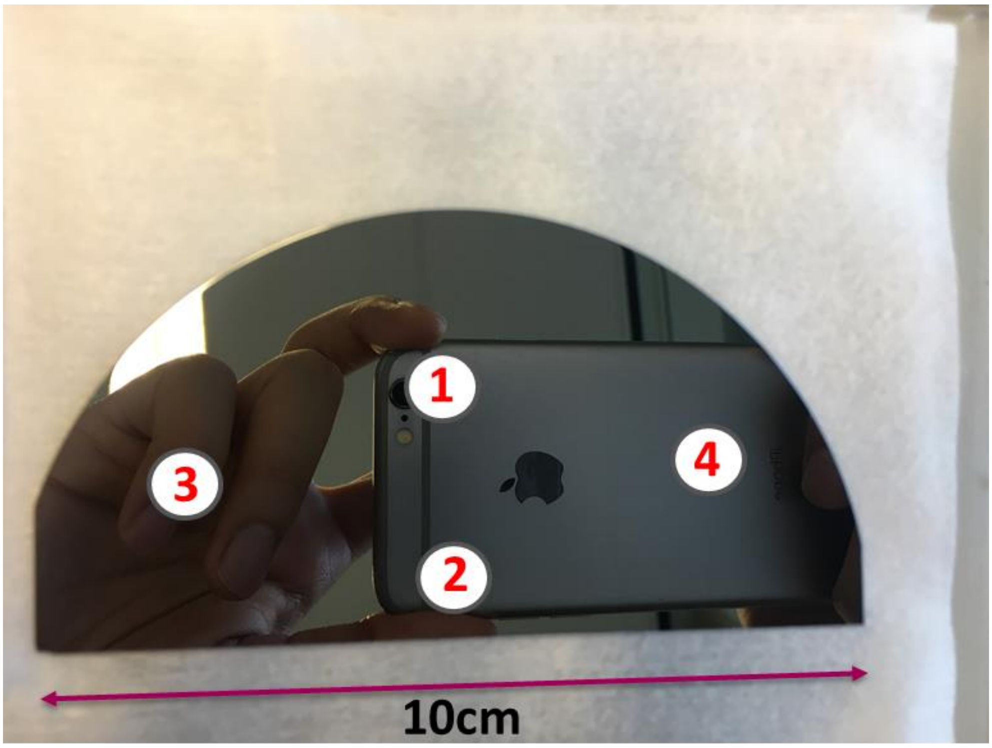

Figure 4.1 (i)a-Si:H thickness measurement on one side of a half wafer

The measured effective lifetime τ_{eff}, implied V_{OC} (iV_{OC}) and thickness of the symmetrical passivated samples are plotted as a function of DR in Figure 4.2. It is worth noting that the surface passivation of c-Si induced by the (i)a-Si:H is thickness-dependent [71], especially when the (i)a-Si:H layer is thinner than 10 nm. Therefore, aim at having a fair comparison between different passivation qualities as results of changed (i)a-Si:H deposition conditions, we first check the deposition rate by depositing the (i)a-Si:H layer on glass or wafer, then calculate the deposition time for the desired thickness for passivation tests.

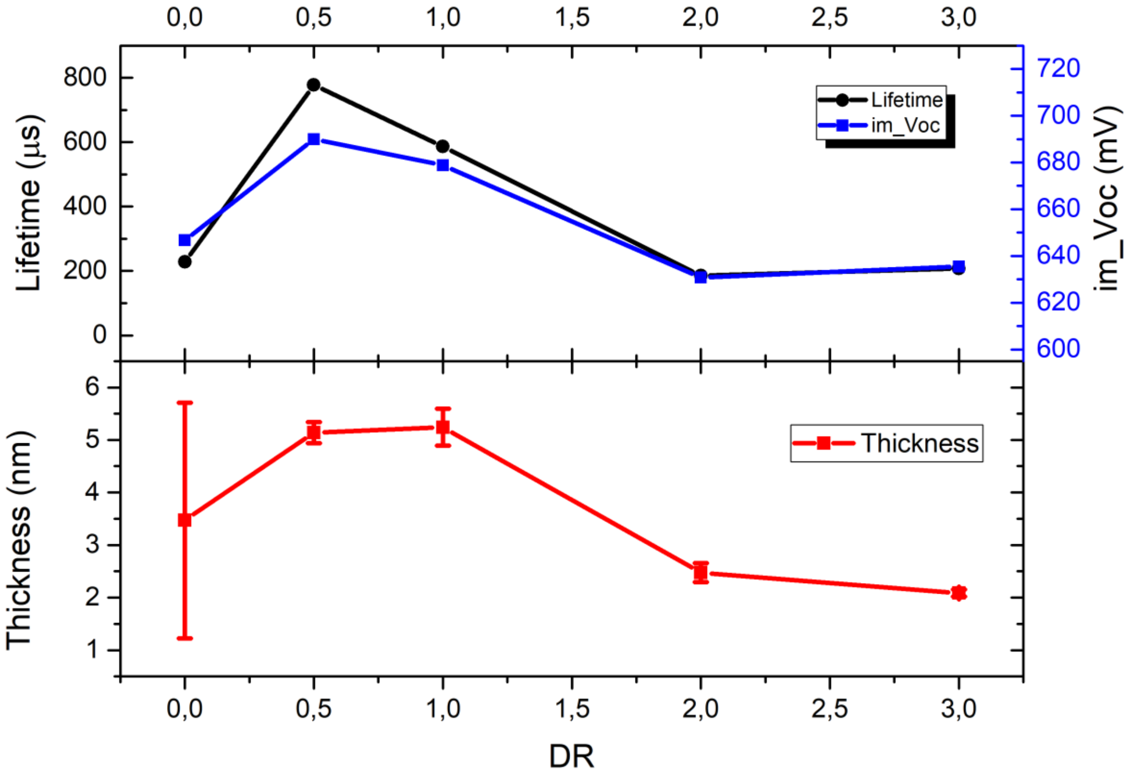

Figure 4.2 The effective lifetime, implied open-circuit voltage and layer thickness as a function of dilution ratio

The target thickness of the (i)a-Si:H layer is 5 nm, however, as shown in Figure 4.2, the eventual thickness of the deposited (i)a-Si:H was varied from 2 nm to around 5.5 nm. When DR = 0, the deposition duration is 110 s, i.e. DR = 0 (110 s), the average thickness is about 3.5 nm, but the error bar is very large, which indicates the growth of (i)a-Si:H by pure SiH_4 on <100> oriented flat surface is not stable. Slight increments of DR from 0 to 0.5 (39 s) and 1 (36s) exhibit deposited thickness of around 5 nm. Passivation quality of τ_{eff} improves from 227 µs to 778 µs and 587 µs, while the iV_{OC} improves from 647 mV to 690 mV and 679 mV for DR = 0.5 and 1, respectively. This range of DR indicates a more appropriate condition of forming a high-quality a-Si/c-Si interface. When DR goes beyond 1, i.e. DR = 2 (33 s) and DR = 3 (37 s), both the thickness and passivation quality drop. This phenomenon agrees with the observation reported by Hao et al. [72] and Hsiao et al. [73]. They observed that with the increase of DR, the (i)a-Si:H experiences a transition from amorphous to crystalline and the passivation quality of c-Si surface will become worse due to the crystalline silicon growth in the deposited films [74]. Dao et al. [75] reported that the transition happens when DR is around 1. At this stage, the deposited (i)a-Si:H is still an amorphous network but contains the high H_2 and the low microstructure factor R. Microstructure of the thin film is determined by the infrared absorption measurement, which reflects the amount of hydrogen-bonded structure. R is defined as the ratio of integrated intensities of 2070 cm^{-1} centered mode and the sum intensities of 2000 cm^{-1} and 2070 cm^{-1} centered modes. R is derived in $R = \frac{I[2070]}{I[2000] + I[2070]}$ 4-2.

$$R = \frac{I[2070]}{I[2000] + I[2070]} \tag{4-2}$$

The I[2070] and I[2000] represents hydrogen multi bonded mode and hydrogen singly bonded mode. Lower R indicates a lower density deficiency (void fraction) [76]. The improved microstructure shows the best passivation quality and also might lead to lower light-induced degradation [77].

As mentioned before, the passivation qualities is found to be closely related to the thickness of the (i)a-Si:H passivating layer as illustrated in Figure 4.2. However, with similar thickness around 5 nm for both DR = 0.5 and DR = 1, the sample with DR = 1 already exhibit degraded passivation quality as compared to that of DR = 0.5. Therefore, we expect less performed (i)a-Si:H passivation quality even when the thicknesses of (i)a-Si:H layer with DR >1 are realized. Overall, (i)a-Si:H layer with DR = 0.5 at thickness around 5 nm can achieve τ_{eff} of 778 µs and iV_{OC} of 690 mV. Meanwhile, this (i)a-Si:H layer offers also a rather uniform deposition. So DR = 0.5 is chosen for the following optimizations.

4.2.2 Effect of Deposition Power

In this section, the deposition power is discussed. Table 4.2 shows the PECVD deposition parameters, the deposition power was ranged from 2.4W to 3.6W, and the designed thickness of (i)a-Si:H is 5 nm.

Table 4.2 PECVD deposition parameters of (i)a-Si:H with varied deposition power

Layers	Substrate Temperature (°C)	Pressure (mbar)	Flow rate (sccm)	Frequency (MHz)	Power (W)	Dilution Ratio (-)
(i)a-Si:H	180	1.4	40	13.56	***2.4-3.6***	0.5

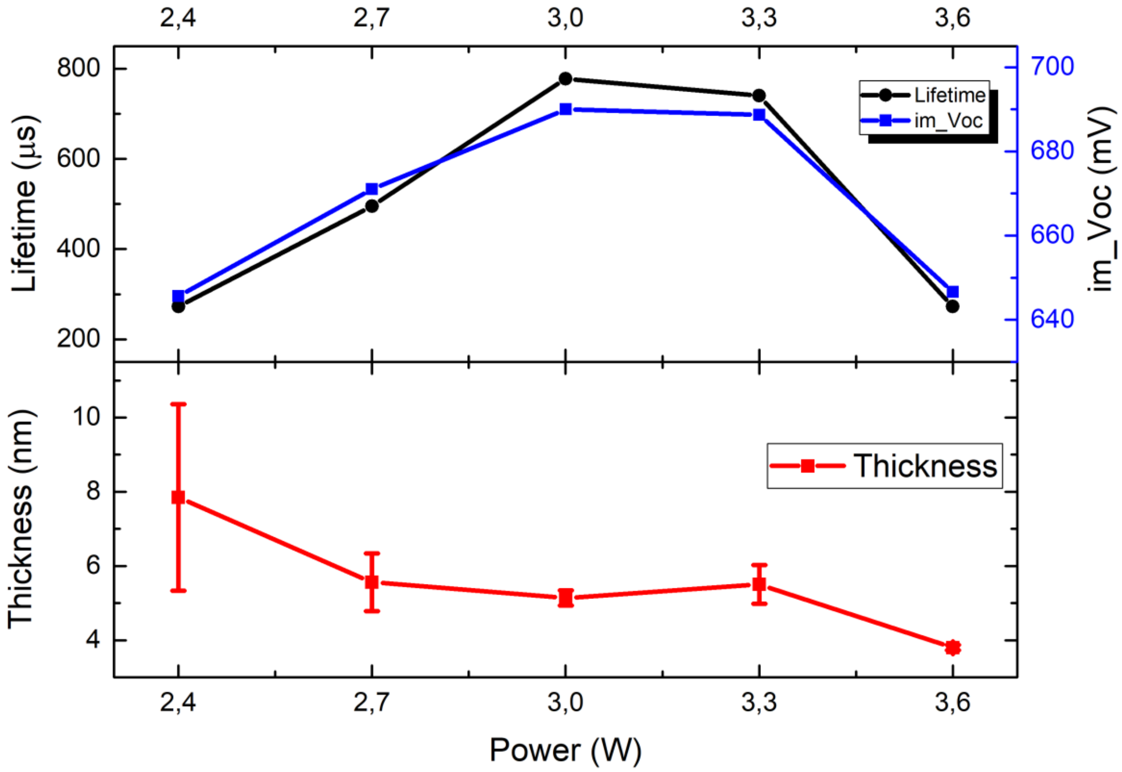

Figure 4.3 The effective lifetime, implied open-circuit voltage and layer thickness as a function of deposition power

Figure 4.3 shows the passivation results of symmetrical passivated samples with (i)a-Si:H featuring different deposition power. From power = 2.4W (180s) to power = 3W (60s), the average thickness of (i)a-Si:H layer decreases from around 8 nm to 5.5 nm, while both of the surface uniformity and passivation characteristics are improved. This can be explained by a higher growth rate and also a denser thin film as a result of a higher applied deposition power [78]. Power = 3W (60s) can achieve the highest τ_{eff} of 777.84 µs and iV_{OC} of 690 mV. With further increase of the power to 3.3W (49 s) and 3.6W (36 s), we observe the degraded passivation qualities for both cases, and also less controlled thickness especially for the sample with 3.6 W deposition power. Therefore, considering both the best passivation quality and also the uniformity of the deposited (i)a-Si:H layer, we choose the deposition power of 3 W for the following optimizations.

So based on the above experiments, the optimized as-deposited single (i)a-Si:H layer (i1) shows in Table 4.3.

Table 4.3 The passivation performance of optimized i1 layer

Layers	τ_{eff} (µs)	iV_{OC} (mV)	Thickness (nm)
i1	777.8	690	5.6

4.2.3 Effect of Hydrogen Plasma Treatment (HPT) Power on the single (i)a-Si:H layer

So far as seen from our optimized single (i)a-Si:H layer, the best passivation quality achieved is still moderate as compared to those reported in the literature [70] [79] [80]. We realize to achieve a decent passivation quality, the direct application of highly hydrogen diluted precursor gases for passivating <100> flat wafer might not be sufficient. Therefore, post-treatment such as HPT as reported in the literature is also explored in this study for improving the passivation quality of c-Si/(i)a-Si:H interface. The working principle of HPT is to inject sufficient hydrogen into the (i)a-Si:H layer and the diffused hydrogen will arrive at the c-Si/(i)a-Si:H interface to saturate the dangling bonds [81]. This treatment leads the (i)a-Si:H layer getting closer to the amorphous to crystalline transition region [82] and thus achieving better passivation [72][73].

In this section, HPT with different power is applied on a 9 nm single (i)a-Si:H layer (80 s). The deposition condition shows in Table 4.4.

Table 4.4 HPT deposition parameters with varied deposition power on a single (i)a-Si:H layer

Layers	Substrate Temperature (°C)	Pressure (mbar)	Flow rate (sccm)	Frequency (MHz)	Dilution Ratio (-)	Duration (s)	Power (W)
i1	180	1.4	40	13.56	0.5	80	3
HPT	180	1.6	200	13.56	/	20	***5-9***

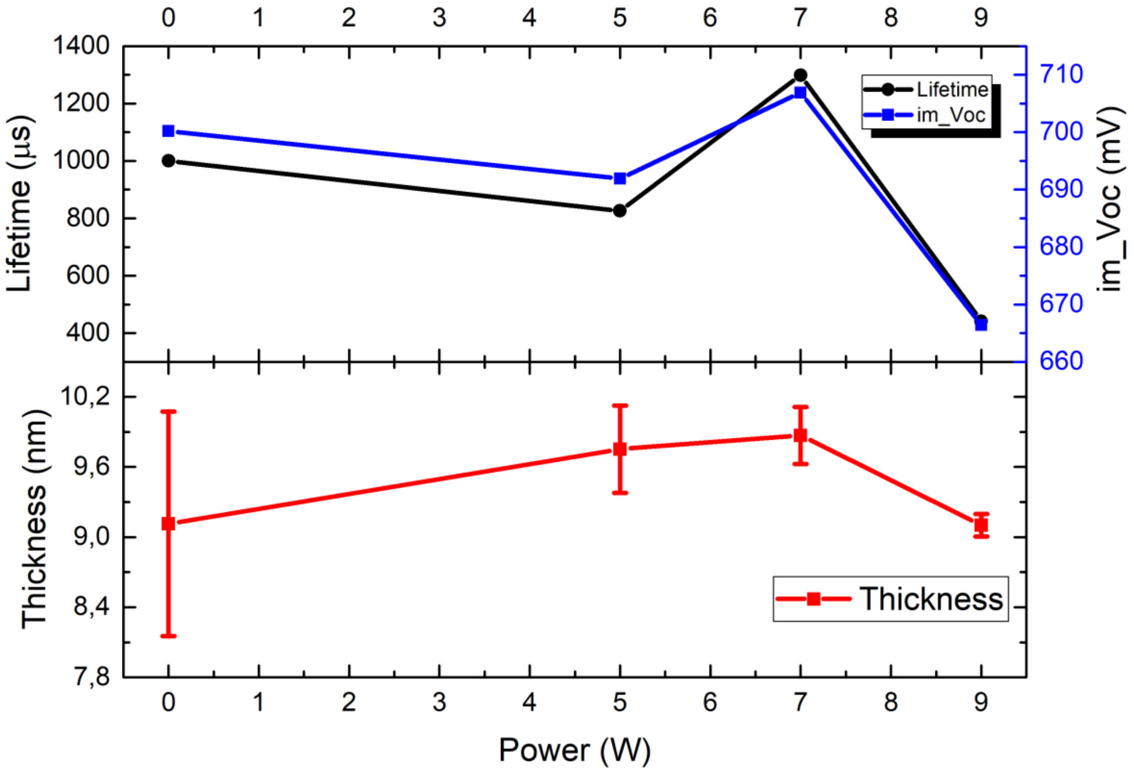

Figure 4.4 The effective lifetime, implied open-circuit voltage and layer thickness as a function of HPT power on a single (i)a-Si:H layer

Figure 4.4 shows the passivation qualities of the symmetrical (i)a-Si:H passivated samples under HPT with different power. We put here the 0 W HPT case as the reference, and to control the thermal budget, this sample is also used to experience the same thermal annealing as those samples with HPT. After the application of HPT, the thickness of i1 layers increases [81]. The upper graph shows the passivation performances. When the HPT power is 7 W, compared to the reference sample with the as-deposited i1 layer, both τ_{eff} and iV_{OC} increase. The τ_{eff} improves from 1000.2 to 1299 µs and iV_{OC} increases from 700.2 to 706.9 mV. But when the power is 5 W, the passivation is worse than the reference sample. This may be explained by a higher power, i.e. 7 W dissociates hydrogen molecules more sufficiently in plasma, thus more diffused hydrogen inside the thin film bulk can saturate more dangling bonds. However, the further increased power deteriorates passivation, just as power at 9 W shows. The τ_{eff} and iV_{OC} go through a drastic reduction, ending with 441.68 µs and 666.4 mV. Too high power forces the hydrogen plasma to bombard the interface and leaves defects [83], which is not the ideal condition for post-treatment. From the thickness graph, we can see the expected etching effect [84] is not so obvious, which might be because the duration of HPT is only 20 s.

4.2.4 Effect of HPT Duration on the single (i)a-Si:H layer

Then we investigate the HPT duration under 7 W. The deposition condition shows Table 4.5. The only variable is the duration, which varies from 0 to 100 s.

Table 4.5 HPT deposition parameters with varied deposition duration on a single (i)a-Si:H layer

Layers	Substrate Temperature (°C)	Pressure (mbar)	Flow rate (sccm)	Frequency (MHz)	Dilution Ratio (-)	Power (W)	Duration (s)
(i)a-Si:H	180	1.4	40	13.56	0.5	3	80
HPT	180	1.6	200	13.56	/	7	***0-100***

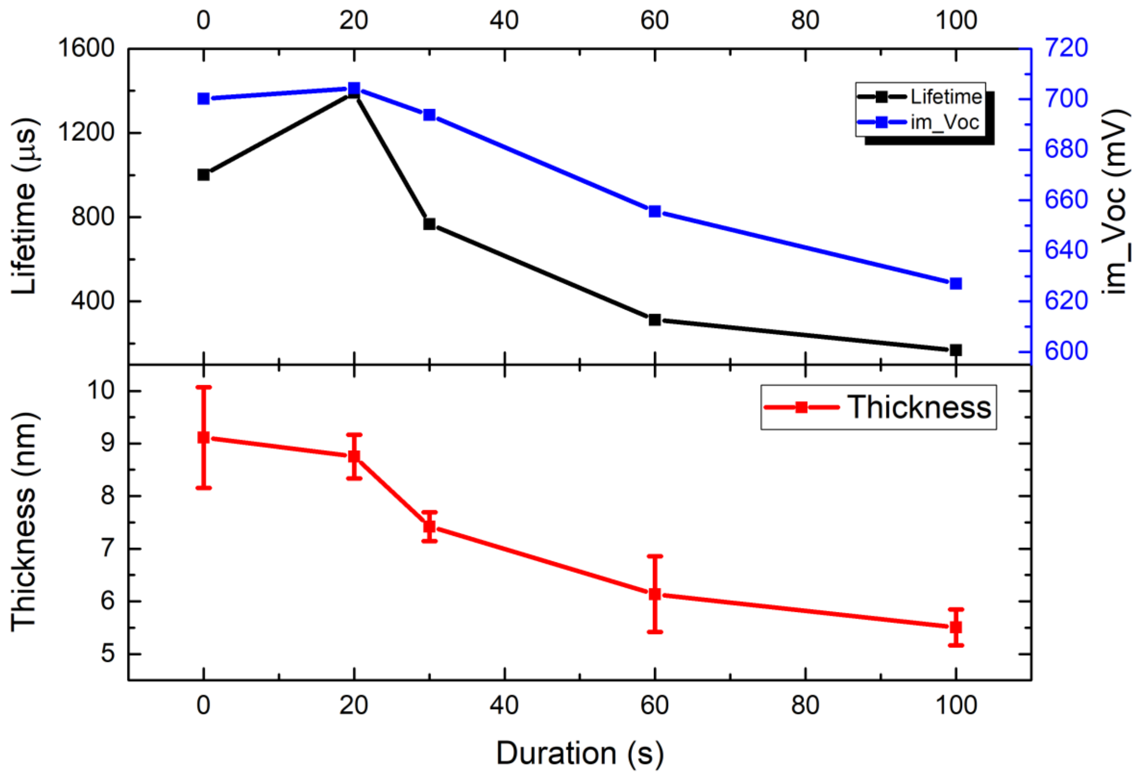

Figure 4.5 The effective lifetime, implied open-circuit voltage and layer thickness as a function of HPT duration on a single (i)a-Si:H layer

The thickness graph of Figure 4.5shows a significant etching effect with increased HPT duration. When the duration is 20 s, the average thickness decreased from 9.1 nm to 8.7 nm, the τ_{eff} and iV_{OC} increased from 1000 to 1391 µs and from 700 to 704.3 mV, respectively. With extended HPT over 30 s, the thickness of the (i)a-Si:H passivating layer keeps reducing, and this is directly correlated with the reductions of τ_{eff} and iV_{OC}. This might because the accumulated H plasma will damage the interface and destroy passivation [84]. Thus, the optimized duration of HPT is 20 s.

By depositing 80 s i1 layer and 20 s HPT under 7 W, the best passivation shows in Table 4.6.

Table 4.6 The passivation performance of optimized HPT on i1 layer

Layers	τ_{eff} (µs)	iV_{OC} (mV)	Thickness (nm)
i1 + HPT	1391	704.3	8.8

4.3 (i)a-Si:H bilayer passivation

To further improving surface passivation, the bilayer structure is applied. The bilayer is a two-step deposition strategy. Compared to the single (i)a-Si:H passivating layer, the bilayer can form a more abrupt interface with less local crystallization and less contained strains, and it can also ensure the effect layer thickness of (i)a-Si:H and improve the passivation [85].

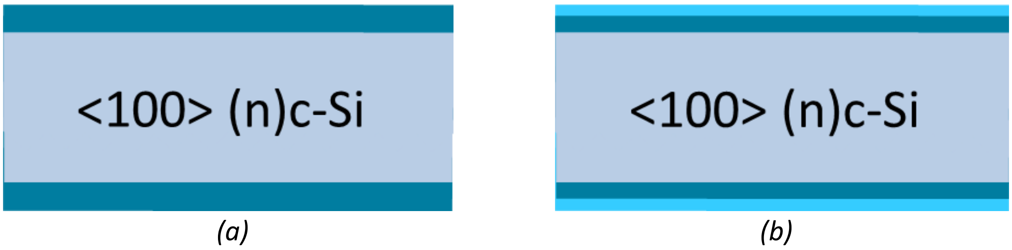

Figure 4.6 Illustration of symmetric passivation layer by using (a) single (i)a-Si:H layer and (b) bilayer structure

Figure 4.6 (a) shows a normal symmetric single (i)a-Si:H passivation layer on flat surfaces, Figure 4.6 (b) illustrates the bilayer structure, which consists of two layers (i)a-Si:H_1 (i1) and (i)a-Si:H_2 (i2). Table 4.7 contains the deposition parameters of these two layers. The i1 layer is the optimized single-layer previously. Compared to the i1 layer, the i2 layer is more hydrogen diluted and it is designed as the optimized passivation layer for <111> oriented wafer [69].

Table 4.7 Deposition parameters of bilayer structure

Layers	Substrate Temperature (°C)	Pressure (mbar)	Flow rate (sccm)	Frequency (MHz)	Dilution Ratio (-)	Power (W)
i1	180	1.4	40	13.56	0.5	3
i2	180	1.4	64	13.56	3	3.2

4.3.1 Bilayer composition

To build a bilayer, we firstly determined the thickness of each layer. We designed different thickness ratios of i1 to i2 layer under a fixed total thickness around 15 nm as described in Table 4.8.

Table 4.8 Deposition parameters during investigating bilayer composition

	Set 1	Set 2	Set 3	Set 4	Set 5	Set 6
Thickness_i1 (nm)	15	10	7.5	5	3	0
Thickness_i2 (nm)	0	5	7.5	10	12	15
Thickness Ratio(i1/i2)	/	2	1	0.5	0.25	0

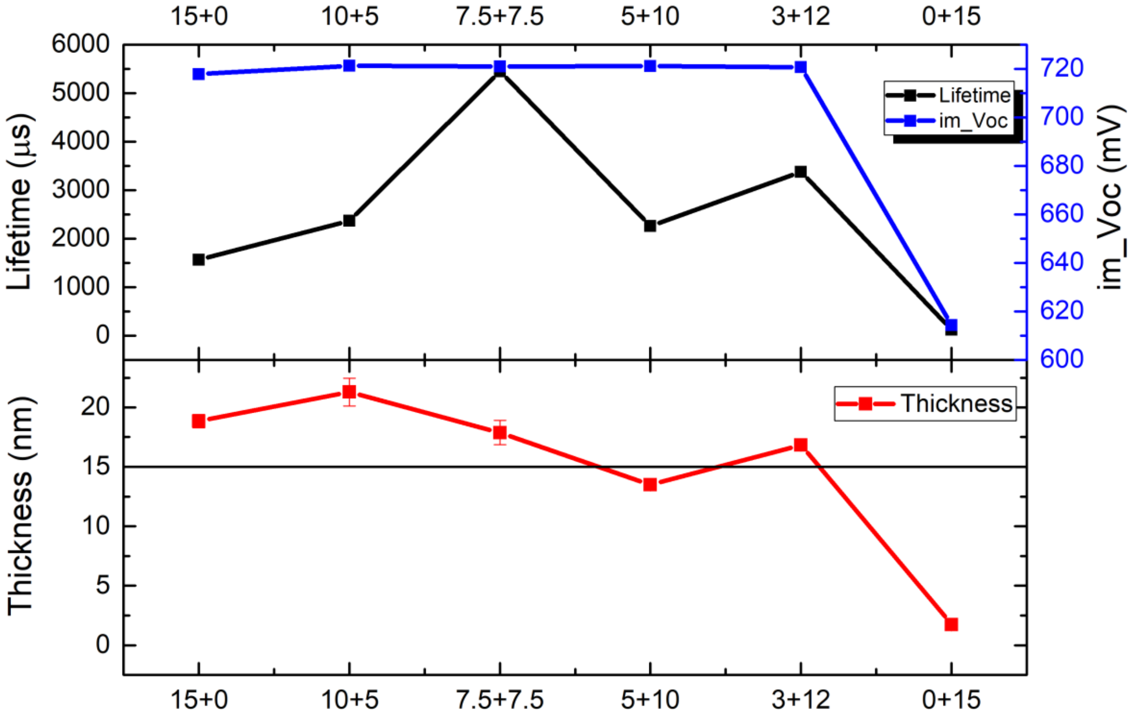

Figure 4.7 The effective lifetime, implied open-circuit voltage and layer thickness as a function of different bilayer composition

Figure 4.7 illustrates the thickness and passivation of different bilayer composition. As we can see, the total thickness of the bilayer deviates from 15 nm, but one may notice the very thin layer of 1.6 nm deposited with set 6 conditions. As set 6 is growing single i2 layer on <100> flat surface, this indicates that highly hydrogen diluted precursor gases are hard to grow an a-Si layer on <100> surface, and instead, it might induce the epitaxial growth that reduces the effective (i)a-Si:H thickness [85].

As for passivation performance, the iV_{OC} is quite similar to each set except set 6. The highest τ_{eff} is 5449.5 µs by using a 7.5 nm i1 layer + 7.5 nm i2 layer. Compared to the single i1 layer(set 1), all the bilayer structures(set 2, 3, 4, 5) can improve the τ_{eff}. This trend shows the advantages of the bilayer structure.

It is well known that the thinner (i)a-Si:H layer leads to less parasitic absorption [86] and less resistive collection of charge carriers [87]. Therefore, 15 nm (i)a-Si:H layer is considered too thick to be applied in solar cells. After determining the composition ratio of the bilayer, we attempted to ensure good passivation under a thinner (i)a-Si:H layer by optimizing the composition in a thinner total thickness.

Thus, we reduced the total layer thickness from 15 to 8 nm by proportionally reducing the deposition duration of i1 and i2 layers. Therefore, the corresponding deposition duration of i1 layer reduced from 80 s to 43 s, and for i2 layer varies from 43 s to 24 s.

Then we investigated the thickness effect of i1 layer. As shown in Table 4.9, i2 layer with a deposition duration of 24 s gives around 5 nm thickness.

Table 4.9 Deposition parameters during investigating i1 layer duration

Layers	Substrate Temperature (°C)	Pressure (mbar)	Flow rate (sccm)	Frequency (MHz)	Power (W)	Dilution Ratio (-)	Duration (s)
i1	180	1.4	40	13.56	3	0.5	***20-43***
i2	180	1.4	64	13.56	3.2	3	24

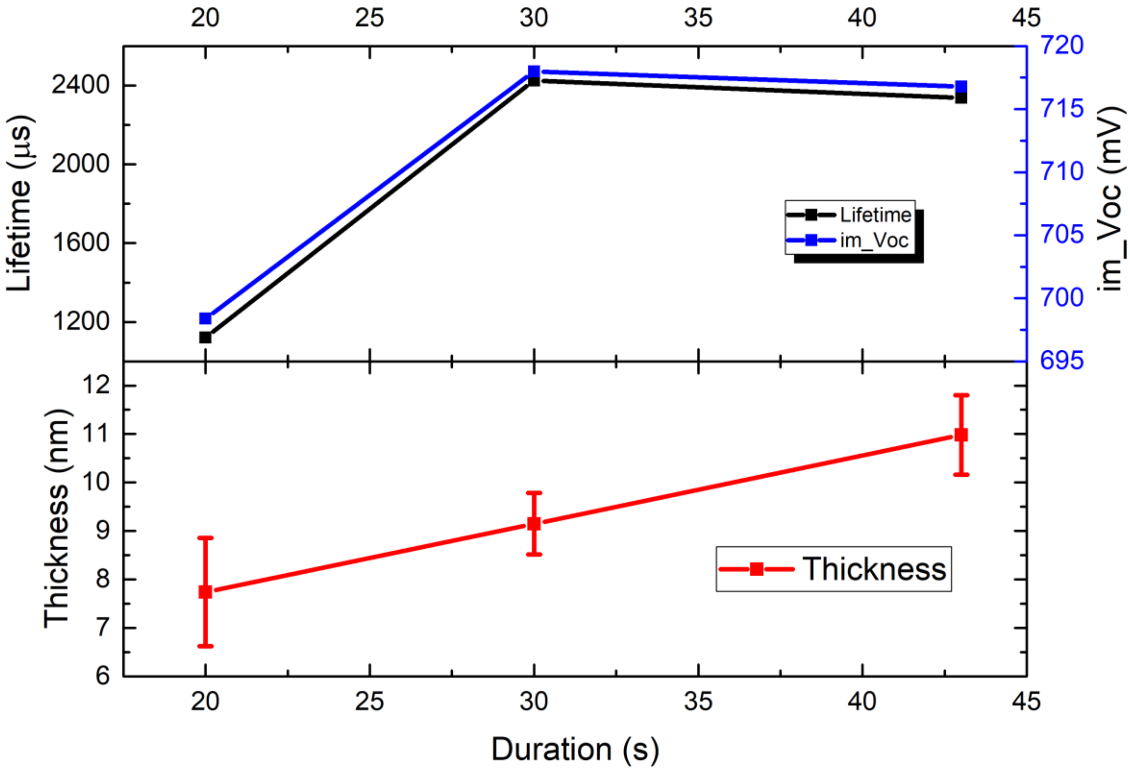

Figure 4.8 The effective lifetime, implied open-circuit voltage and layer thickness as a function of i1 layer duration

Figure 4.8 illustrates the bilayer passivation and total thickness results. Both duration of 43 s(6 nm) and 30 s(4 nm) leads to good passivation. The best passivation happens at a duration of 30 s, which leads to a bilayer total thickness of 9 nm, the τ_{eff} is 2425.52 µs and iV_{OC} is 718 mV. When the deposition duration of i1 layer decreases to 20 s, the τ_{eff} and iV_{OC} drops to 1121 µs and 698 mV, respectively. The total thickness is less than 8 nm, as for i1 layer the thickness is thinner than 3 nm, which is too thin to become a “buffer layer” for the highly hydrogen-diluted i2 layer, thus, i2 layer deposition could damage the interface [88]. So in an as-deposited bilayer structure, too short deposition duration of i1 layer (thinner than 3 nm) results in insufficient passivation quality for the bilayer structure.

The thickness demonstrates a linear fitting with deposition time, which reflects a uniform growth of i1 layer, the growth rate of i1 layer is

$$R_{i1} = 0.14\, nm/s.$$

To keep finding out the optimized layer composition and reducing the total thickness, the duration of the i2 layer is going to be tuned just as given in Table 4.10. The duration of the i1 layer is 30 s (~4 nm) for all the sets, and the duration of i2 layers varies from 0 to 24 s.

Table 4.10 Deposition parameters during investigating i2 layer duration

Layers	Substrate Temperature (°C)	Pressure (mbar)	Flow rate (sccm)	Frequency (MHz)	Power (W)	Dilution Ratio (-)	Duration (s)
i1	180	1.4	40	13.56	3	0.5	30
i2	180	1.4	64	13.56	3.2	3	***0-24***

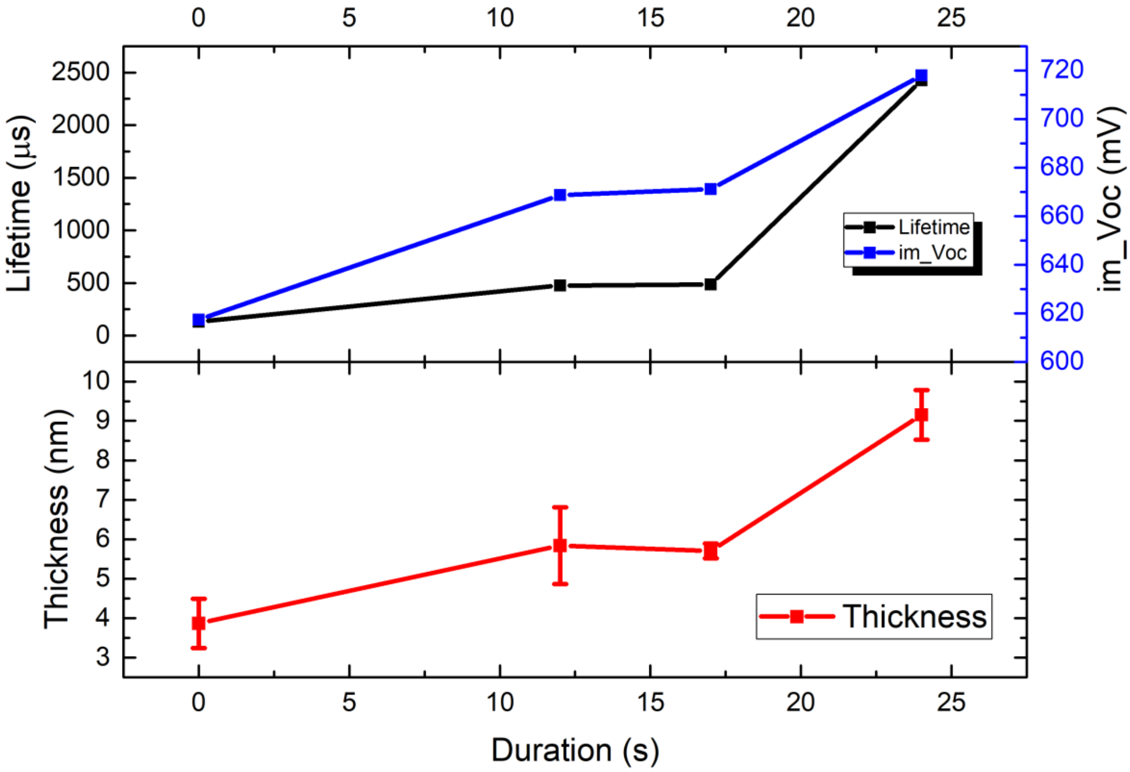

Figure 4.9 The effective lifetime, implied open-circuit voltage and layer thickness as a function of i2 layer duration

Figure 4.9 shows the passivation and total thickness of the bilayer structure under a different duration of the i2 layer. When the duration increases from 0 to 12 s, the τ_{eff} improves from 132 µs to 475 µs and iV_{OC} increases from 617 mV to 669 mV. During 12 to 17 s, the τ_{eff} and iV_{OC} experience a plateau. When the duration comes to 24 s, both τ_{eff} and iV_{OC} improve significantly to 2426 µs and 718 mV, respectively. This result turns out that the thickness of the i2 layer is very critical to passivation, too thin of i2 layer disallow bilayer working functionally [85] [89].

The thickness graph shows a similar trend to passivation, the growth rate for the i2 layer is slower at first 12 s, from 12 to 17 s there is no obvious change in the total thickness. This could be blamed on the experiment errors, and if we look at the bottom of the error bar it shows a linear relationship between growing thickness and deposition duration. During 17 to 24 s, the growth of the i2 layer becomes faster. Thus, we obtained a growth rate for i2 layer:

$$R_{i2} = 0.14\, nm/s \quad (first\ 2\ nm) \tag{4-3}$$

$$R_{i2} = 0.34\, nm/s \quad (after\ 2\ nm) \tag{4-4}$$

4.3.2 Effect of HPT bilayer structure

To keep reducing the bilayer thickness, instead of shortening the duration of either i1 or i2 layer, HPT is applied since the etching effect can reduce the thickness, meanwhile, it may improve further the passivation quality.

In this part, we consider the effect of both HPT power and deposition order. The power in this experiment is set as 3.5 W, 5 W, and 7 W. As for the deposition order, HPT is applied after the i1 layer or after the i2 layer. The former one is called pre-HPT and the latter one is post-HPT.

Table 4.11 shows the deposition parameters. Since in 4.2.4 HPT duration on single (i)a-Si:H (9 nm) is 20 s, considering the thickness of i1 layer is only around 4 nm and the one variable principle, the duration of both HPT is 10 s.

Table 4.11 Deposition parameters during investigating pre/post-HPT effect on bilayer structure

Layers	Substrate Temperature (°C)	Pressure (mbar)	Flow rate (sccm)	Frequency (MHz)	Dilution Ratio (-)	Power (W)
i1	180	1.4	40	13.56	0.5	3
Pre-HPT	180	1.6	200	13.56	/	***3.5-7***
i2	180	1.4	64	13.56	3	3.2
Post-HPT	180	1.6	200	13.56	/	***3.5-7***

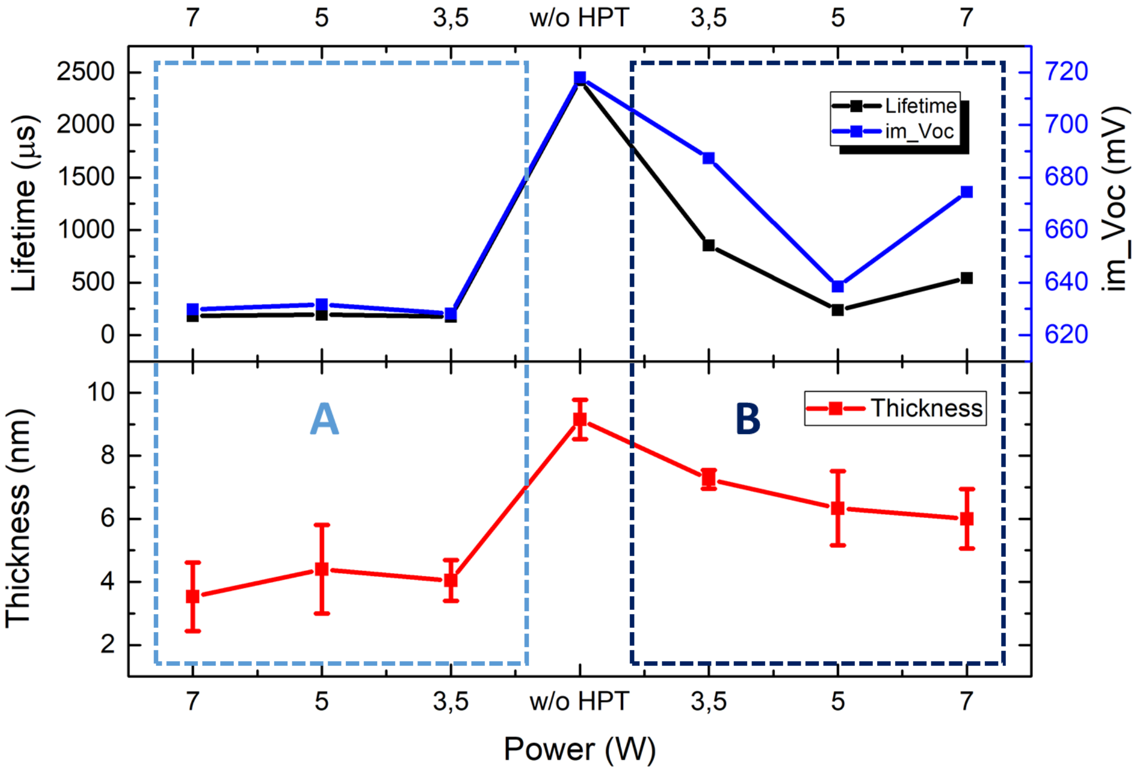

Figure 4.10 The effective lifetime, implied open-circuit voltage and layer thickness as a function of pre/post-HPT power. Area A represents pre-HPT and area B represents post-HPT

Figure 4.10 shows the thickness and passivation under different HPT power and order. The first three sets in area A are pre-HPT and the three sets in area B are post-HPT. The thickness shows that under HPT, the etching effect is significant, the total thickness of pre-HPT is thinner than post-HPT, which means that the etching rate of the i1 layer is faster than the i2 layer. As for passivation, it illustrates that either pre-HPT or post-HPT destroyed the passivation of the as-deposited bilayer. The pre-HPT of different power leads to a similar τ_{eff} around 200 µs and iV_{OC} below 650 mV. The total thickness is around 4 nm, which means the i1 layer might be totally etched by pre-HPT, and HPT probably directly works on the c-Si surface, which could damage the surface. Later the high hydrogen-diluted i2 layer will deposit on the <100> oriented flat c-Si surface, which can easily induce epitaxial growth and reduce the effect (i)a-Si:H film thickness. As for the post-HPT, the etching effect on the i2 layer is not as fast as the i1 layer and in the end, left 2-3 nm i2 layer, but the post-HPT can still degrade the as-deposited bilayer passivation, which is not what we expected.

4.3.3 Effect of HPT duration on bilayer structure

Since 30 s i1(4 nm) seems not appropriate to any HPT, a thicker i1 layer under 43 s(6 nm) is chosen to test the HPT duration. The test condition shows in Table 4.12, the duration of HPT varies from 0 to 50 s.

Table 4.12 Deposition parameters during investigating pre-HPT duration on bilayer structure

Layers	Substrate Temperature (°C)	Pressure (mbar)	Flow rate (sccm)	Frequency (MHz)	Power (W)	Dilution Ratio (-)	Duration (s)
i1	180	1.4	40	13.56	3	0.5	43
HPT	180	1.6	200	13.56	7	/	***0-50***
i2	180	1.4	64	13.56	3.2	3	24

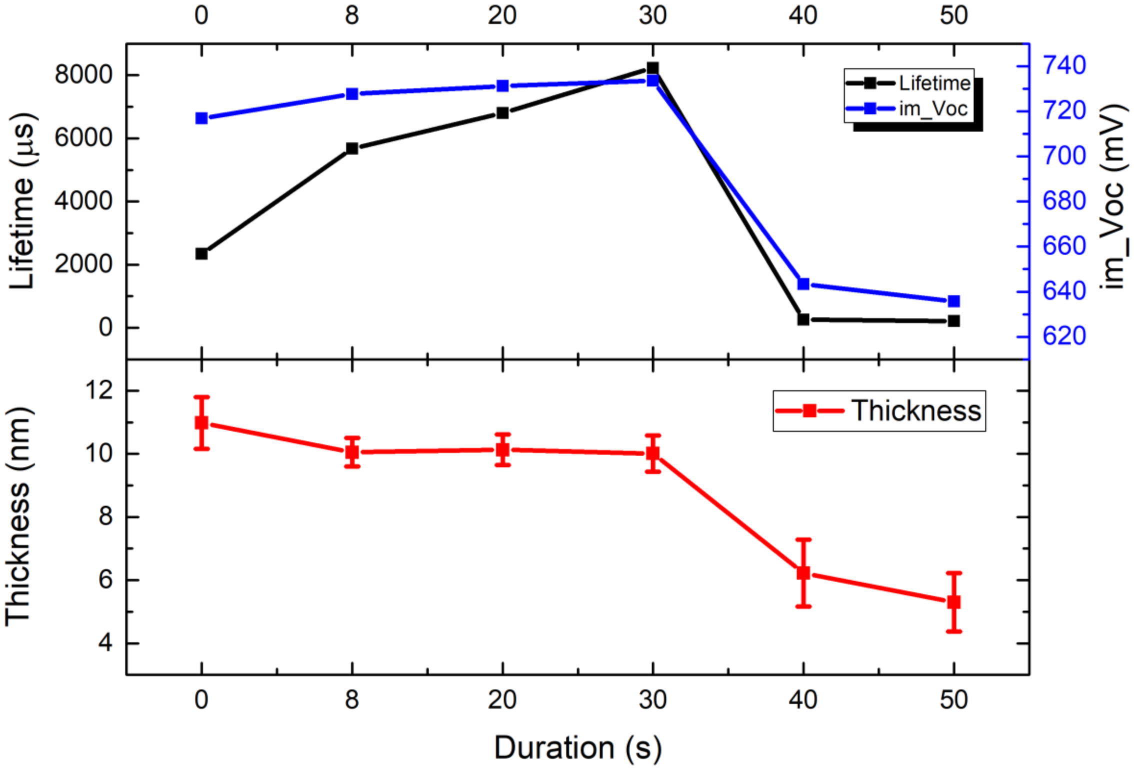

Figure 4.11 The effective lifetime, implied open-circuit voltage and layer thickness as a function of pre-HPT duration

Figure 4.11 illustrates that in the first 30 s, the passivation gets better and better with the increased HPT duration. Also, there is a slightly etching effect in the first 30 s. After 30 s, the etching effect becomes significant but together with significant drops of the passivation quality. This indicates the accumulated HPT has exceeded the threshold that the i1 layer can buffer.

The best passivation performance by the optimized bilayer shows in Table 4.13.

Table 4.13 The passivation performance of optimized bilayer structure

Layers	τ_{eff} (μs)	iV_{OC} (mV)	Thickness (nm)
i1+HPT+i2	8228.7	733.5	10

4.4 Summary

In this chapter the optimization (i)a-Si:H layers is conducted. The criteria of optimization are surface passivation results (τ_{eff} and iV_{OC}) and surface uniformity. Both single (i)a-Si:H and bilayer structure show thickness-dependent passivation and by applying pre/post-HPT the as-deposited (i)a-Si:H passivation can get improvement. There are several types of (i)a-Si:H layers that are ready to be applied in the FBC-SHJ solar cell fabrication.

Chapter 5 FBC-SHJ SOLAR CELLS

This chapter discusses the fabrication of single-side textured FBC-SHJ solar cells, including the fabrication process and different composition of intrinsic and doped layers.

5.1 Fabrication Process

The flow chart of single-side textured FBC-SHJ solar cells contains the following steps:

- Wafer single-side SiN_x deposition
- Wafer single-side texture (5% TMAH)
- 20 minutes BHF (1:7) immersion
- Wet-chemical cleaning (3 times)
- Flat/textured side full area (i)a-Si:H passivation (AMOR)
- Flat side full area n-type layer deposition (AMIGO)
- Textured side full area p-type layer deposition (AMIGO)
- Front and rear side patterned ITO deposition
- Front and rear side silver screen printing

The substrate is FZ n-type <100> oriented c-Si wafer with resistivity 1-5 Ωcm and thickness of 280 ± 20 µm. Step 1 is to deposit around 200 nm SiN_x layer as a masking layer, which will protect the front flat side from TMAH etching [90]. Step 2 is to form the textured rear side by using TMAH, the height of random pyramids is in range of 1-4 µm. Step 3 is to remove the SiN_x masking layer by BHF treatment due to the etching of a weak Si-N bond [91]. Step 4 is 3 times standard wet-chemical cleaning, which is a so-called nitric acid oxidation cycle (NAOC) [92]. This process consists of immersing wafers into nitric acid to form SiO_x thin films, and subsequent HF will etch the SiO_x layer away. It leads to a reduced defect density at the interface, which is important for cell device performance [93]. Step 5 is to deposit (i)a-Si:H passivation layers on the pre-processed wafer. A variety of optimized (i)a-Si:H layers in chapter 4 will be applied. Step 6 is to deposit n-type layers on the front-flat side, both n-type amorphous silicon ((n)a-Si) layer and n-type hydrogenated nanocrystalline silicon ((n)nc-Si:H) layer are applied. Step 7 is to deposit p-type layers on the rear-textured side. The p-type layers consist of 4 nm (p)nc-SiO_x layer and 16 nm (p)nc-Si layer, these layers have been optimized on the textured side wafer by Y. Zhao [94]. Step 8 is to deposit ITO on both sides of the wafer, either patterned area on the front-flat side or the rear-textured side. The thickness of the front side and the backside is 75 nm and 150 nm, respectively.

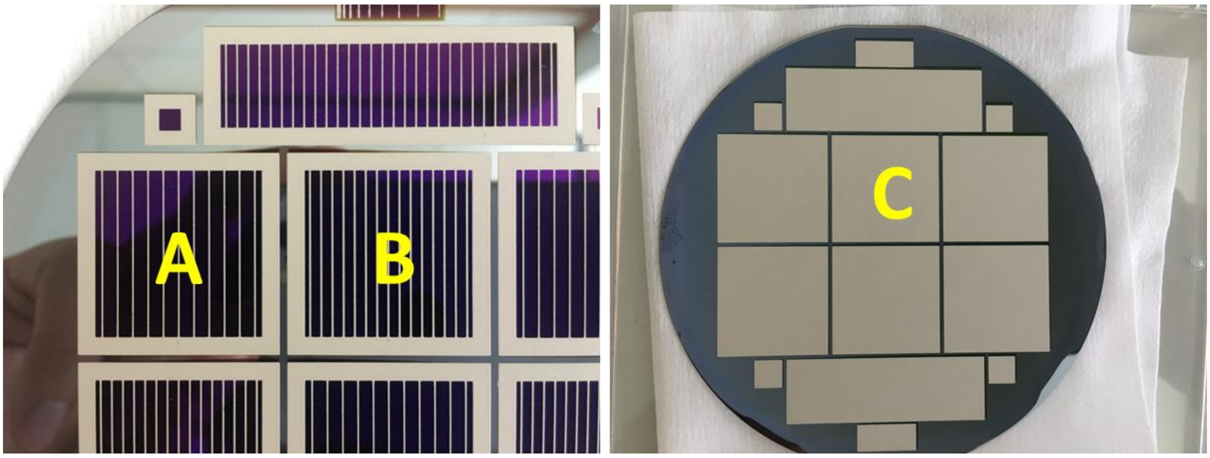

Figure 5.1 Screen printing pattern. For the front side, A is 4.4% metal coverage and B is 7.5% metal coverage; for the rear side, C is the full area metal coverage

Step 9 is metallization by screen printing as Figure 5.1 shows, there are 2 patterns for the front side, either 4.4%, and 7.5% metal coverage. As for the rear side, full area metallization is applied.

5.2 Single-side textured FBC-SHJ solar cell

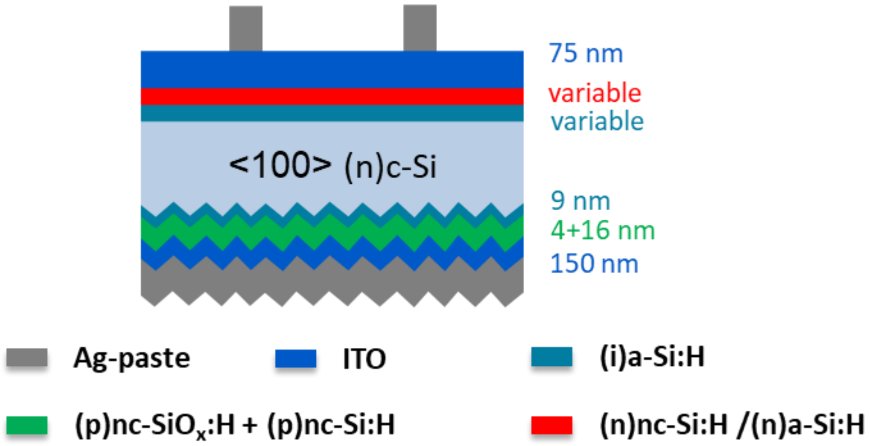

Figure 5.2 The illustration of single side-textured front-back contacted heterojunction solar cell structure

Figure 5.2 shows the FBC-SHJ solar cell structure. It is a rear junction solar cell [95], which follows the n-i-p architecture of perovskite top cell, which can gain the optical advantages. Figure 5.2 also illustrates the corresponded layer thickness, for the front side, both (n)-type layer and (i)a-Si:H the optimized thicknesses are variable, which will be discussed in the following section.

In this chapter we combine varied (i)a-Si:H layers with (n)nc-Si:H and (n)a-Si layer to optimize the solar cell performance.

5.3 Single-side textured FBC-SHJ solar cell with (n)nc-Si:H layer

Table 5.1 shows the deposition parameters of (n)nc-Si:H, which contains a very high H_2 flow rate. This is because the presence of hydrogen can facilitate the layer transition from disorder to order, which is known as hydrogen-induced crystallization [82]. The hydrogen highly diluted precursor gas can also etch the a-Si layer, the deposited (i)a-Si:H needs to be durable enough to resist H impinge.

Table 5.1 Deposition parameters of (n)nc-Si:H layer

Layers	Substrate Temperature (°C)	Pressure (mbar)	Power (W)	SiH_4 (sccm)	PH_3 (sccm)	H_2 (sccm)
(n)nc-Si:H	180	1.4	11	1	1.2	100

5.3.1 Optimization of (n)nc-Si layer thickness

To optimize the thickness of (n)nc-Si, there are three sets of thickness: 13 nm, 8 nm, and 3 nm. Different (n)nc-Si:H layers are applied on a bilayer structure composed by 3.2 nm i1 and 4.8 nm i2.

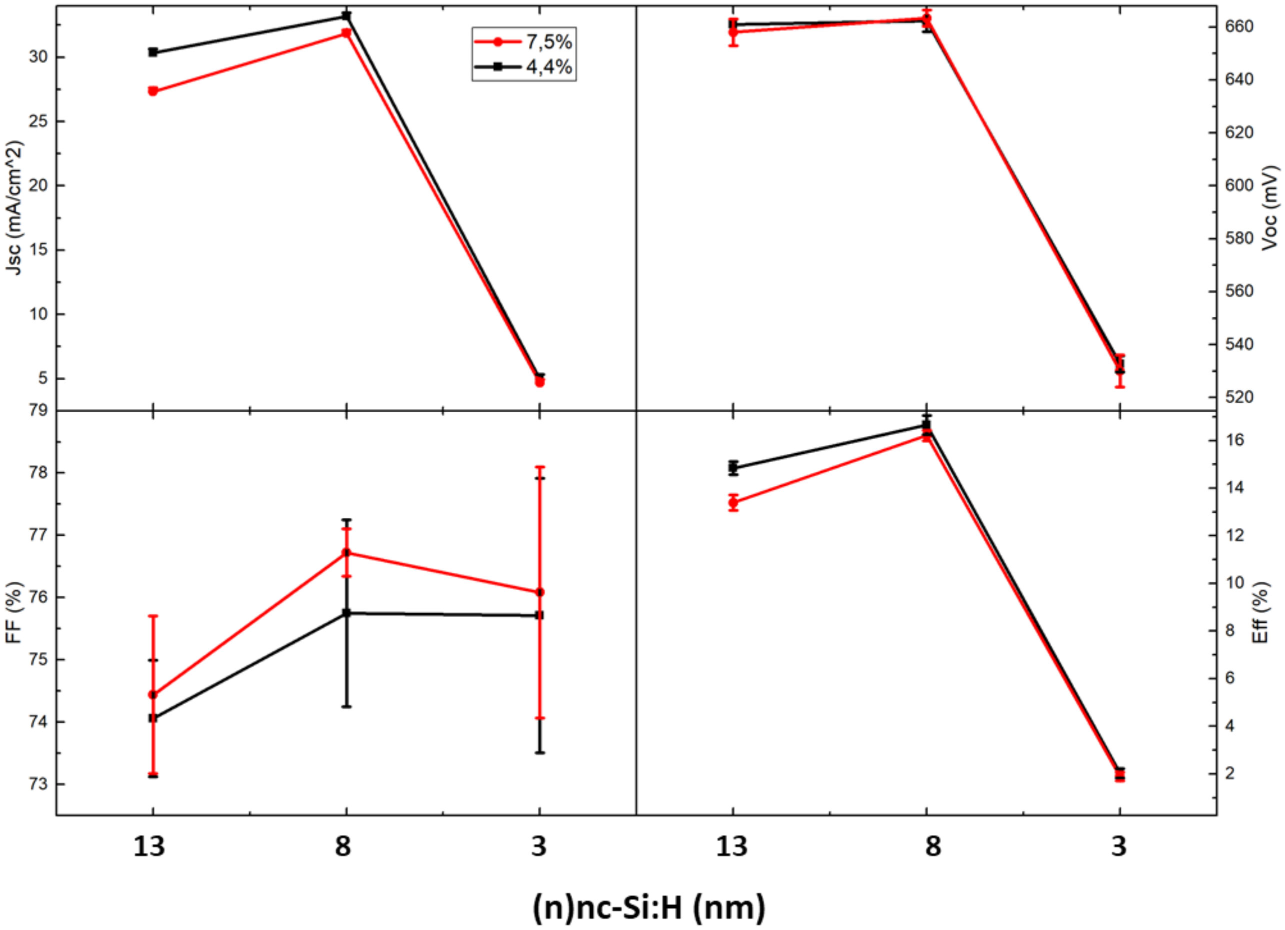

Figure 5.3 The J-V parameters of solar cells as a function of different (n)nc-Si:H layer thickness.

Figure 5.3 illustrates solar cell performance. When the thickness is 13 nm, either the *FF* or J_{sc} is less than 8 nm under both metallization patterns. As for *FF* that could be explained by the series resistance, In general, thicker (n)nc-Si:H layer has higher lateral conductivity that is beneficial for FF, but still maybe the resistance effect with higher thickness is more dominant, because the layers are rather amorphous. So there might be a kind of trade-off. And for J_{sc} that is because the bandgap and absorption coefficient of (n)nc-Si:H are higher than c-Si, when it sited on the front side, the incident light will first go through the (n)nc-Si:H layer, which will cause parasitic absorption. Thicker (n)nc-Si:H layer leads to higher parasitic absorption loss. When the thickness comes to 3 nm, there is a significant drop in V_{OC} because of the ITO damage, the passivation and efficiency of the solar cell cracks, as it shows that the efficiency is less than 2%. This could be explained by too thin (n)nc-Si:H layer can’t resist the ion bombardment during ITO sputtering. Thus, the c-Si interface will suffer from the deterioration, and the passivation destroyed.

When the thickness of (n)nc-Si:H is 8 nm, both V_{OC} and FF are the best among the series. So 8 nm is chosen for the following experiments.

5.3.2 The symmetric bilayer composition

Table 5.2 shows the applied (i)a-Si:H layer. In this section, a symmetric structure of (i)a-Si:H layers is applied in passivation. Random pyramids form the rear-textured side, increasing the related surface area. Thus, the layer growth rate on the textured side is lower. To ensure the same (i)a-Si:H layer thickness on both sides of c-Si substrate, a time ratio of 1.7 is applied, which means the growth rate of the thin layer on the textured side is 1.7 times slower than the flat side.

Table 5.2 Deposition parameters of symmetric passivation layers with (n)nc-Si:H layer

Sample	Passivation layer (front-flat)	Passivation layer (rear-textured)
Set1	43s_i1+24s_i2	73s_i1+41s_i2
Set2	43s_i1+8s_HPT+24s_i2	73s_i1+14s_HPT+41s_i2
Set3	43s_i1+10s_HPT+24s_i2	73s_i1+17s_HPT+41s_i2
Set4	43s_i1+20s_HPT+24s_i2	73s_i1+34s_HPT+41s_i2

The basic passivation structure is as-deposited 43s i1 + 24s i2 (~11 nm) bilayer, and from set1 to set4, the utilization of pre_HPT increases, which is expected to result in a hydrogen-riched (i)a-Si:H layer that is beneficial to surface passivation [96].

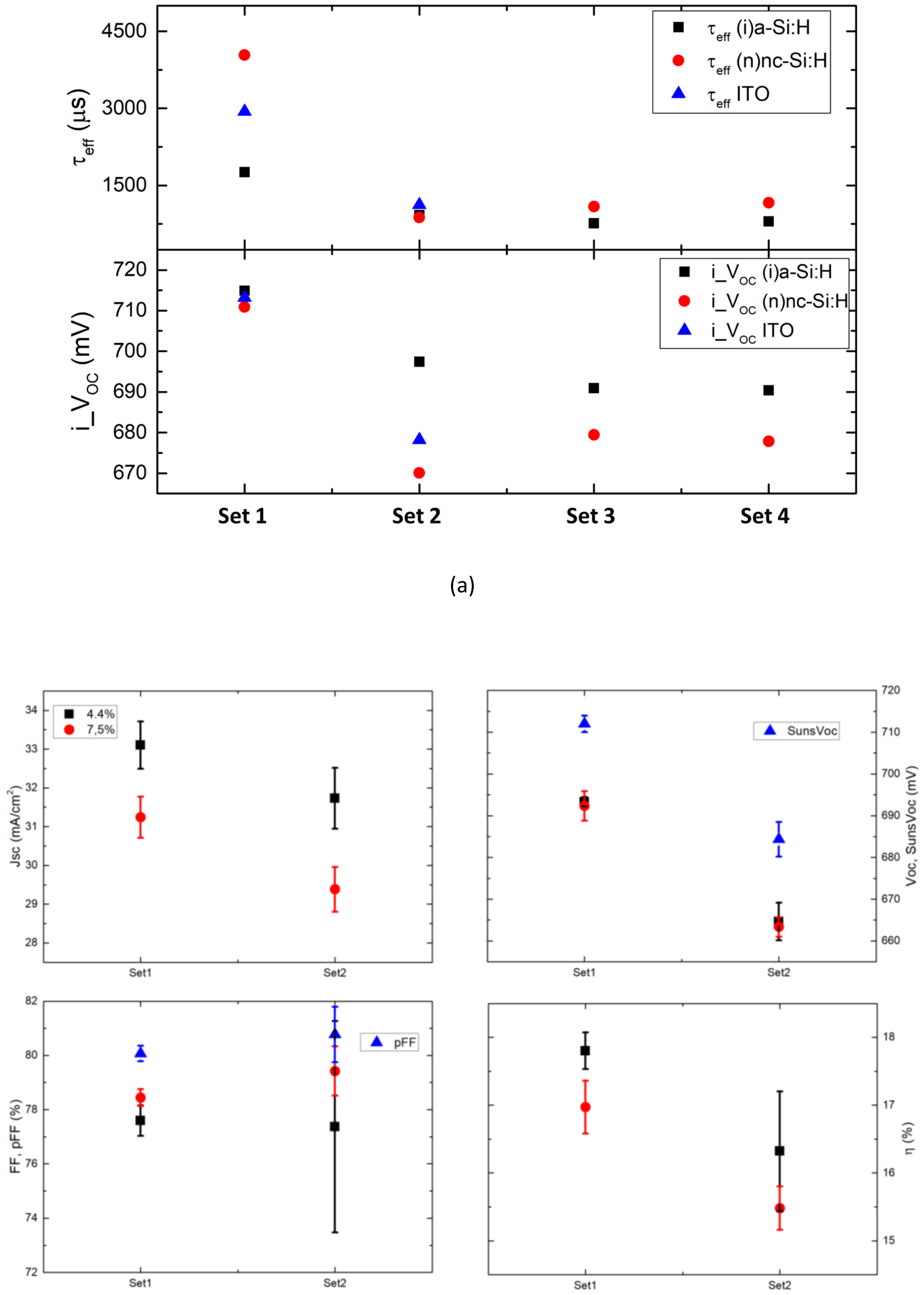

(a)

(b)

Figure 5.4 (a) The effective lifetime, implied open-circuit voltage; (b) The J-V parameters of solar cells as a function of different HPT on symmetric bilayer with (n)nc-Si:H

As for the passivation, Figure 5.4 (a) illustrates the iV_{OC} and τ_{eff} at different processing steps. For intrinsic layer passivation, set1 achieves the best passivation, the highest iV_{OC} is 715 mV and the highest τ_{eff} is 1.76 ms. But for set2 to set4, either iV_{OC} or τ_{eff} decreases with extended HPT, and the τ_{eff} is lower than 1 ms. This trend is not what we expected since in Chapter 4 we found that the pre_HPT can improve passivation based on 43s i1+24s i2 bilayer structure, but there shows an opposite trend. This phenomenon points out that there may exist a reproducibility issue in AMOR, and the optimized HPT may not be appropriate to <111> textured surface. After depositing the (n)nc-Si:H and (p)nc-SiO_X:H + (p)nc-Si:H layers, for set2 to set4, the iV_{OC} of all sets decreased significantly while for set1 the iV_{OC} remains at a high level at 710 mV. This could be explained by the deposition condition of (n)nc-Si where the precursor gases are highly hydrogen diluted (DR = 100), so the deposition of (n)nc-Si could be regarded as a post-HPT for the former (i)a-Si:H layer. Compared to other sets, set1 is an as-deposited bilayer structure without pre-HPT, so it has a denser layer that is more resistant to the post-HPT brought by the deposition of (n)nc-Si:H. As for τ_{eff}, most sets get increased after depositing the (n)nc-Si:H and (p)nc-SiO_X:H + (p)nc-Si:H layers, especially for set1, the τ_{eff} comes to 4 ms, which is consistent with the its variety of iV_{OC}. Set1 and set2 are fabricated to solar cells, the ITO sputtering does not affect much on set1, the iV_{OC} remains and the τ_{eff} degrades to 2.9 ms. For set2 the τ_{eff} remains the same level while the iV_{OC} improves, but still lower than (i)a-Si:H passivation.

Figure 5.4 (b) shows the solar cell performance of set1 and set2. There are 2 patterns of metal coverage on the front side, 4.4%, and 7.5%. Generally, a higher metal coverage (7.5%) can facilitate the collection of charge carriers, which mans higher FF. Meanwhile, a lower metal coverage (4.4%) leads to less shading loss, so it is expected to gain higher J_{SC}. In this experiment, under different metal coverage patterns, the V_{OC} is similar to each other. And the final efficiency is higher with the 4.4% metal coverage pattern. Under 4.4% pattern, set1 achieves V_{OC} at 693 mV, J_{SC} at 33.1 mA/cm^2, *FF* at 77.59% and the efficiency at 17.8%. As for set2, under 4.4% pattern, the V_{OC} is 664 mV, the J_{SC} is 31.73 mA/cm^2, *FF* is 77.37% and efficiency is 16.32%. The main differences between these two sets are V_{OC} and J_{SC}. The passivation of set1 is better than set2, thus, so higher V_{OC} is achieved. For J_{SC}, both sets ar applied bilayer (i)a-Si:H and (n)nc-Si:H on the front side, and thickness between set1 (~ 11 nm + 8 nm) and set2 (~ 10 nm + 8 nm) are almost the same, so the difference of J_{SC} could be blamed on the collection probability. Set1 has better passivation, which means less surface recombination and higher collection probability. So we can see the passivation directly affect the V_{OC} and J_{SC}.

5.3.3 The unsymmetric (i)a-Si:H composition

Instead of depositing the same intrinsic layer on both sides, an optimized (i)a-Si:H (i2) layer by Y. Zhao is applied [69]. This designed layer is for textured c-Si passivation. The thickness of the i2 layer is important since it needs to satisfy the good passivation quality and meanwhile less impact on *FF*. In our solar cell fabrication, a 9 nm of i2 layer is accepted, which can supply good passivation and protect the c-Si/(i)a-Si:H interface from being damaged by high-power deposition of (p)nc-SiO_x/(p)nc-Si.

Table 5.3 Deposition parameters of unsymmetric passivation layer with (n)nc-Si:H layer

Sample	Passivation layer (front-flat)	Passivation layer (rear-textured)
Set1	43s_i1+8s_HPT	81_i2
Set2	30s_i1+24s_i2	81_i2
Set3	43s_i1+24s_i2	81_i2
Set4	20s_i1+24s_i2+10s_HPT	81_i2
Set5	43s_i1+30s_HPT+24s_i2	81_i2
Set6	43s_i1+20s_HPT+24s_i2+10s_HPT	81_i2

Table 5.3 shows the (i)a-Si:H layer structures of different sets.

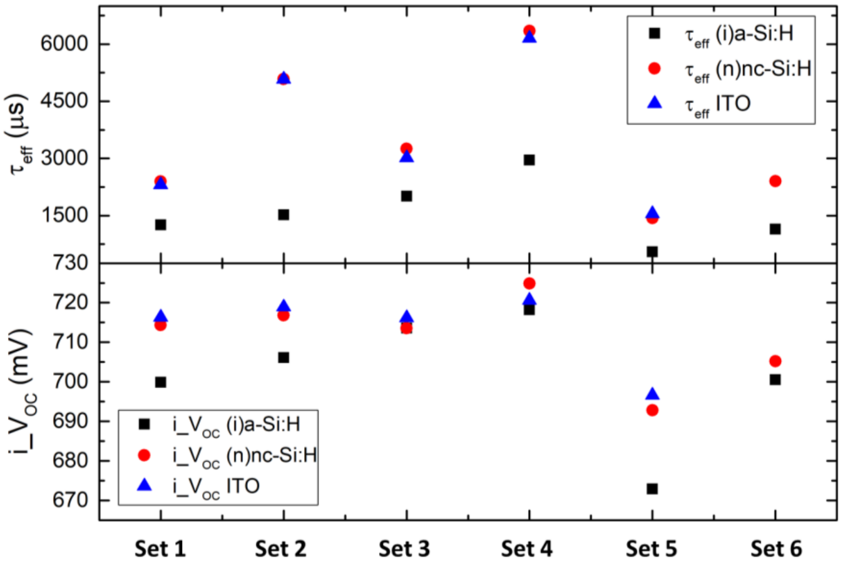

(a)

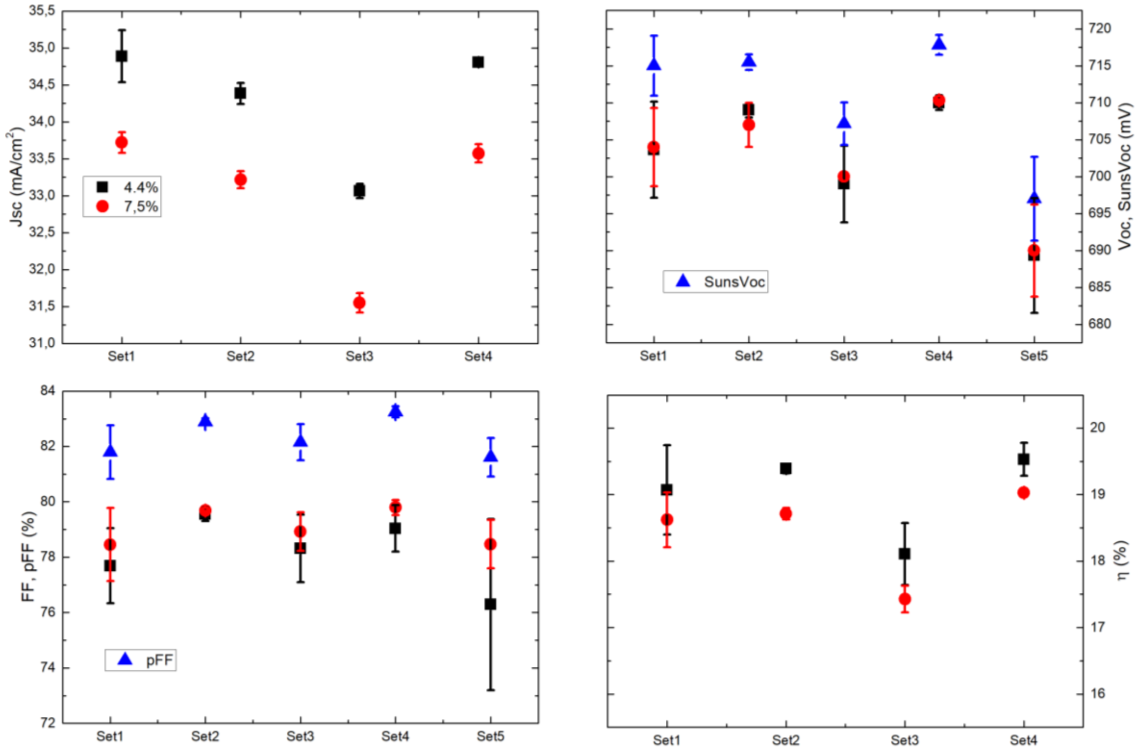

(b)

Figure 5.5 (a) The effective lifetime, implied open-circuit voltage; (b) The J-V parameters of solar cells as a function of different front side bilayer (i)a-Si:H with (n)nc-Si:H

Figure 5.5 (a) demonstrates the passivation performance of different structures. For (i)a-Si:H, the best passivation is achieved by set4 (~ 5 nm), the τ_{eff} is 2.9 ms and the iV_{OC} is 718.2 mV. Set1 front side is as-deposited i1 layer with HPT (~ 5.6 nm), as we demonstrated in section 4.2, symmetrical as-deposited i1 layer with HPT on flat wafer doesn't achieve passivation as good as bilayer structure, but still set1 achieves τ_{eff} at 1.3 ms, iV_{OC} at 700 mV with the help of rear side i2 layer. And since the front side (i)a-Si:H is only 5.6 nm thin, it is expected to achieve higher J_{SC} and FF in the device level. As for set2 (~ 9 nm) and set3 (~ 11 nm), both of them are bilayer but with different i1 layer thickness. The passivation trend follows section 4.3.1 that a thicker bilayer can have better passivation results, set3 with a thicker bilayer can achieve τ_{eff} at 2 ms and iV_{OC} at 713.6 mV. Actually, in the previous section 5.3.2, the best passivation is achieved by using 43s_i1+24s_i2 on the front flat side, which is the same (i)a-Si:H as set3, the τ_{eff} and iV_{OC} are comparable. In this section, on the rear textured side, the thickness of the used single (i)a-Si:H layer i2 is thinner than the bilayer in 5.3.2, which indicates potential in achieving higher FF. As for set5 (~ 10 nm) and set6 (~ 8.5 nm), either pre-HPT or post-HPT deteriorates the passivation on the as-deposited bilayer when compared to set3. These results also point out the repeatability issue in AMOR. After (n)nc-Si:H/(p)nc-SiO$_X$:H+(p)nc-Si:H layer deposition, the passivation for all the sets gets improvement, especially for set2 and set4, the τ_{eff} are 5.1 ms and 6.4 ms, respectively, which indicates the high power HPT doesn't degrade the (i)a-Si:H/c-Si interface passivation. Set1-5 are deposited ITO and fabricated into solar cells, and Figure 5.5(a) also shows that

TCO sputtering doesn't harm the passivation, proving the optimized (i)a-Si:H layer and (n)nc-Si:H layer is resilient to the ITO sputtering.

Figure 5.5(b) illustrates solar cell performance. Under a 4.4% metal coverage, for set2 the V_{OC} is 699 mV, J_{SC} is 33 mA/cm^2, and *FF* is 78.31% and efficiency is 18.1%. Compared to the 5.3.2 set1 under the symmetric structure, the J_{SC} is the same but the V_{OC} and *FF* are higher. This can be explained by a better passivation and thinner rear side (i)a-Si:H layer by using i2 layer. The highest average efficiency is achieved by set4 at 19.53%, also for set1 (19.07%) and set2 (19.39%) are higher than 19%. The improvement compared to section 5.3.2 contains V_{OC}, J_{SC} and *FF*. The V_{OC} increases from 693 to 710 mV, while J_{SC} increases from 33.1 to 34.8 mA/cm^2, also *FF* increases from 77.59 to 79% under 4.4% pattern. These characteristics improvements can be a credit to more excellent passivation of (i)a-Si:H layer, which can be found in Figure 5.5(a), and also the thinner thickness for both front and rear side (i)a-Si:H layers.

5.4 Single-side textured FBC-SHJ solar cell with (n)a-Si layer

The deposition condition of (n)a-Si layer is shown in Table 5.4. The power is 3.2 W and there is no H_2 in the precursor gases, which is a less harsh deposition environment compared to (n)nc-Si deposition. So the less damage on passivation by using (n)a-Si is expected.

Table 5.4 Deposition parameters of (n)a-Si layer

Layers	Substrate Temperature (°C)	Pressure (mbar)	Power (W)	SiH_4 (sccm)	PH_3 (sccm)
(n)a-Si	180	0.6	3.2	40	11

5.4.1 The symmetric (i)a-Si:H composition

For the symmetric structure, there are two sets of passivation layers.

Table 5.5 Deposition parameters of symmetric passivation layer with (n)a-Si layer

Sample	Passivation layer (front-flat)	Passivation layer (rear-textured)
Set1	43s_i1+24s_i2	73s_i1+41s_i2
Set2	43s_i1+8s_HPT+24s_i2	73s_i1+14s_HPT+41s_i2

Table 5.5 illustrates the passivation layer composition, set1 is the as-deposited bilayer structure, while set2 adds 8 s pre-HPT. The duration of the rear textured side is 1.7 times of front flat sie because of the random pyramids.

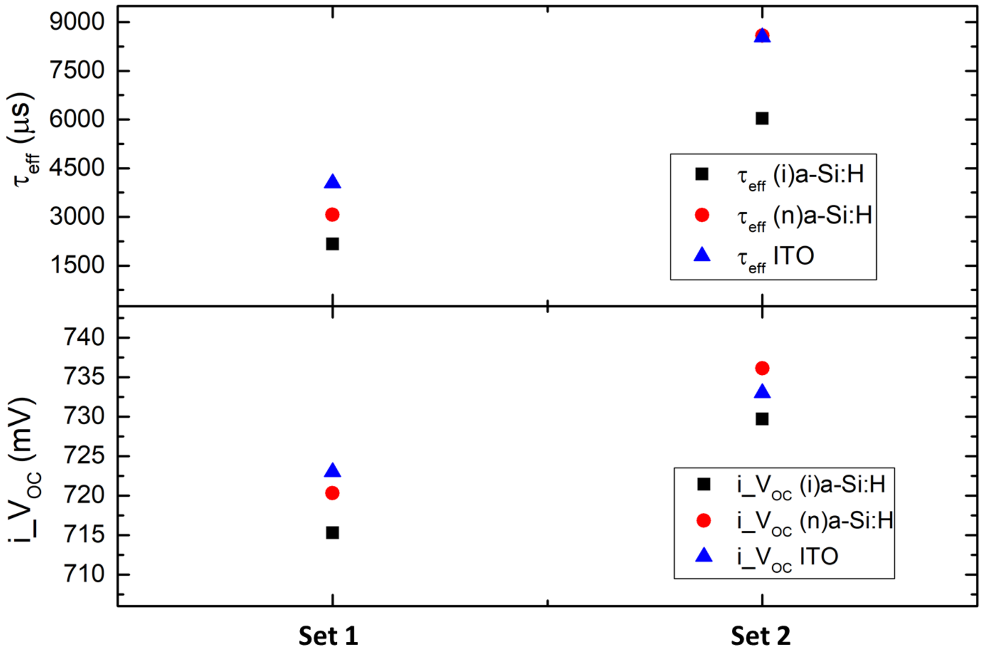

(a)

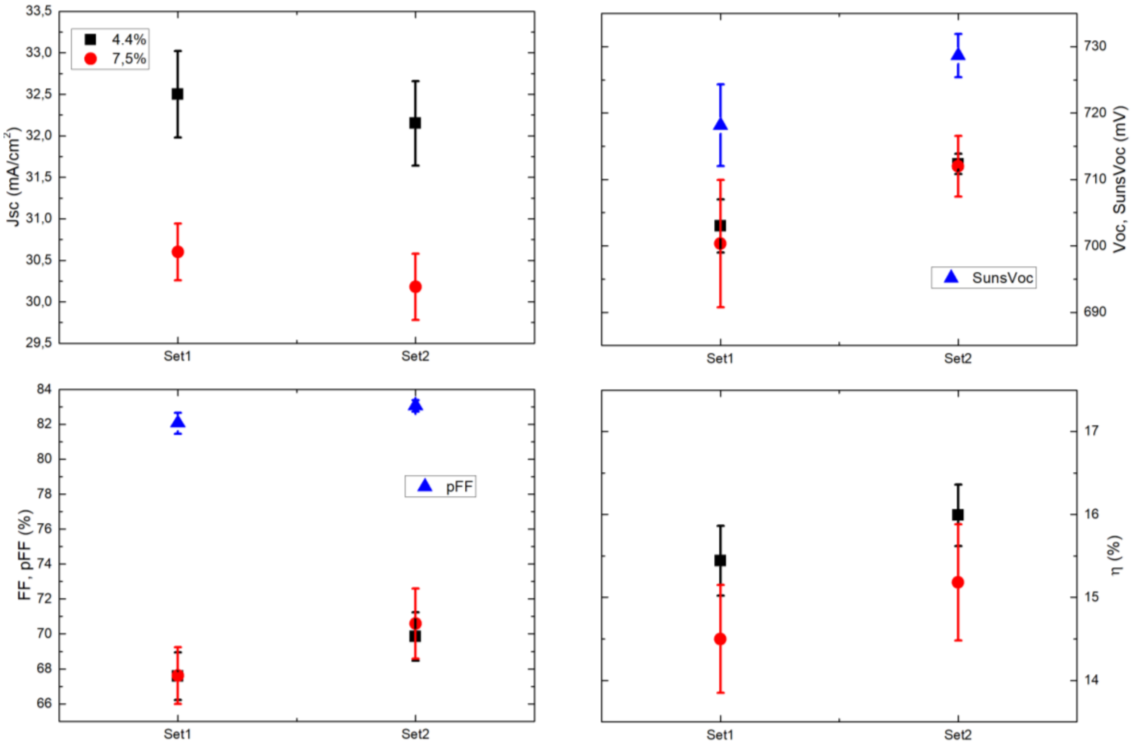

(b)

Figure 5.6 (a) The effective lifetime, implied open-circuit voltage; (b) The J-V parameters of solar cells as a function of different symmetrical (i)a-Si:H with (n)a-Si

Figure 5.6 (a) shows the passivation of two sets. The intrinsic layer passivation is good for both sets, and the results of set1 (~11 nm) are identical to previous sets of using the same structure. This illustrates the form of pure bilayer structure and layer quality is stable. Compared to set1, set2 (~10 nm) achieves better passivation by using pre-HPT, the τ_{eff} is 8.5 ms and iV_{OC} is 730 mV. Indeed, the pre-HPT enhances the passivation, which is exactly what we designed and expected. After the doped layer deposition and TCO sputtering, the passivation gets improved for both sets.

Figure 5.6 (b) presents solar cell performance. For both sets, the V_{OC} are over 700 mV, especially for set2, the V_{OC} is 712 mV under 4.4% metal coverage, while set1 also achieves 703 mV. But the *FF* and J_{SC} are quite low for these two sets. Under 4.4% metal coverage, the J_{SC} of set2 is 32.2 mA/cm^2 and the *FF* is 69.9%. This could be explained by the thickness of (i)a-Si:H layer, since there is no H_2 in (n)a-Si layer deposition. The thickness of (i)a-Si:H is around 11 nm for both set1 and set2. Thus, parasitic absorption plays a role in the loss of J_{SC}. Also the thick (i)a-Si:H may increase the series resistance during the transport of charge carriers, so the *FF* is lower compared to the previous sets. The highest efficiency of set2 is 16.41% with 4.4% metal coverage.

5.4.2 The unsymmetric (i)a-Si:H composition

In this section, we adjust the passivation layer into the unsymmetric structure. The rear side is still a 9 nm i2 layer. The sample sets are shown in Table 5.6.

Table 5.6 Deposition parameters of unsymmetric passivation layer with (n)a-Si layer

Sample	Passivation layer (front-flat)	Passivation layer (rear-textured)
Set1	43s_i1+8s_HPT	81_i2
Set2	30s_i1+24s_i2	81_i2
Set3	43s_i1+30s_HPT+24s_i2	81_i2
Set4	43s_i1+20s_HPT+24s_i2+20s_HPT	81_i2

Based on the previous symmetric passivation layer structure we know that the initial thickness of the front flat side (i)a-Si:H is very important in (n)a-Si doped layer solar cell because there is no external HPT could shrink the (i)a-Si:H layer. So in this series experiment, either we reduce the duration of i1 layer to 30 s or pre/post-HPT is applied.

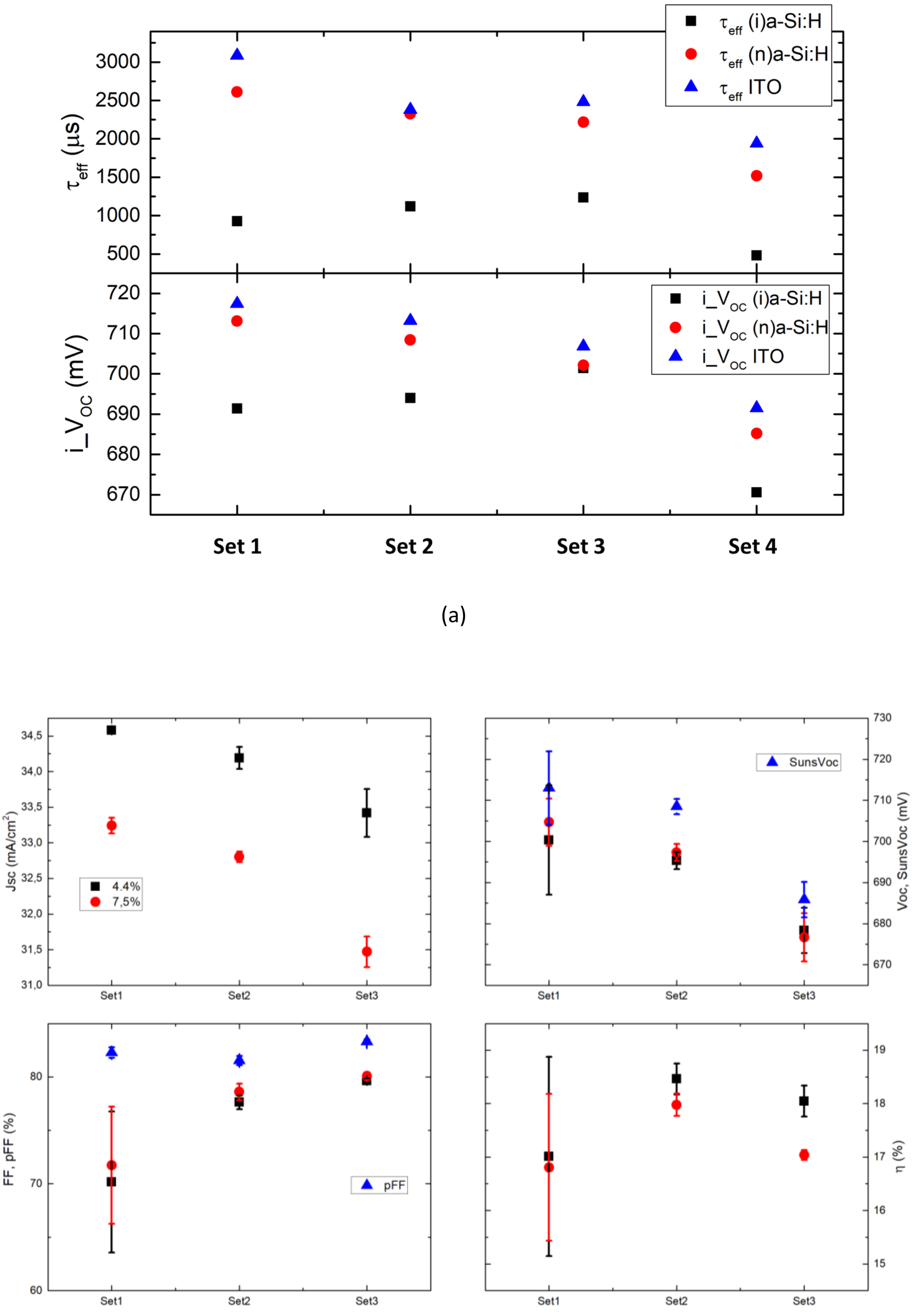

(a)

(b)

Figure 5.7 (a) The effective lifetime, implied open-circuit voltage; (b) The J-V parameters of solar cells as a function of different unsymmetrical (i)a-Si:H with (n)a-Si

Figure 5.7 (a) demonstrates the passivation results. For (i)a-Si:H, set1 with 30 s pre-HPT gets the best passivation. But it is lower than the section 5.3.3 set3 (43s_i1+24s_i2), which indicates that the pre-HPT doesn't work functionally. And in this section, set4 with both 20s pre- and post-HPT achieves the worst passivation, compared to 5.3.3 set6, the unideal passivation might be blamed on the post-HPT is too much for the as-deposited bilayer that deteriorates the (i)a-Si:H/c-Si interface. After (n)a-Si/(p)nc-SiO$_X$:H+(p)nc-Si:H layer deposition and ITO sputtering, the passivation of all sets gets improved, especially for set1 (~ 5 nm), the τ_{eff} increases from 0.9 to 3.1 ms, and iV_{OC} increases from 691.4 to 717.4 mV. Set1 to set3 are fabricated into solar cells.

Figure 5.7 (b) illustrates solar cell performance. Under 4.4% metal coverage, set2 achieves J_{SC} at 34.2 mA/cm^2, V_{OC} at 695 mV, *FF* at 77.6% and the highest efficiency at 18.46%. Set1 has a high V_{OC} over 700 mV and high J_{SC} over 34.5 mA/cm^2, but the *FF* is only around 71% and the error bar is very large, which indicates a none uniform layer. As for set3, the J_{SC} is 33.4 mA/cm^2 and the V_{OC} is around 680 mV, even *FF* is high at 79.6% but the efficiency is around 18% under 4.4 metal coverage. This might result from the poorer passivation compared to set2 as shown in Figure 5.7 (a). There is a significant improvement in J_{SC} and *FF* from section 5.4.1, from 32.2 to 34.2 mA/cm^2 and 69.9% to 77.6%, respectively. These credits are to the thinner (i)a-Si:H for both the front and rear sides.

5.5 Champion cells

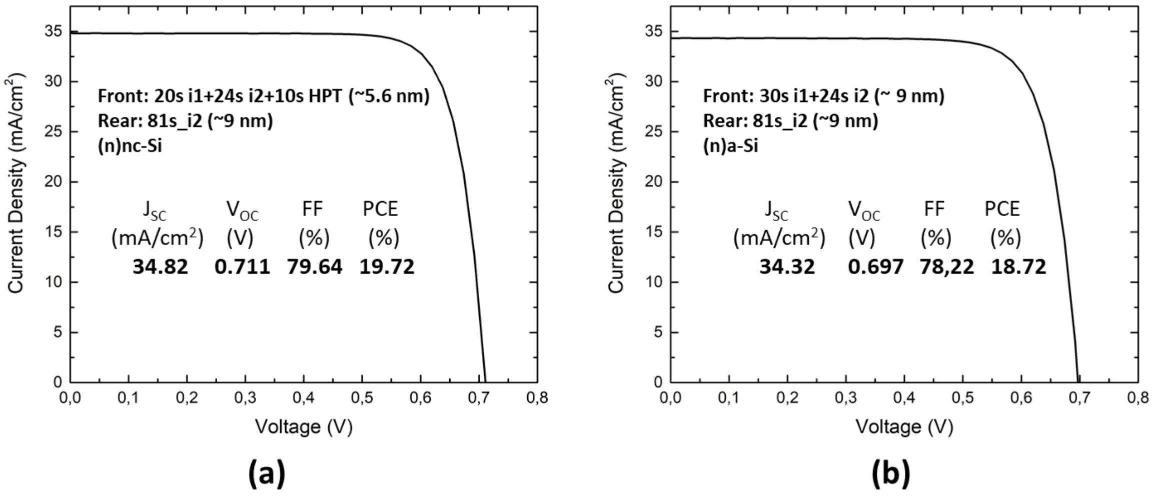

Figure 5.8 The J-V curve of champion cells with n-doped (a) nc-Si:H; (b) a-Si layer

Figure 5.8 presents 2 champion cells. (a) is by using (n)nc-SI:H layer with thin (i)a-si:H layers(front: 20 s i1 + 24 s i2 + 10s HPT; rear: 81 s i2), (b) is achieved by using (n)a-Si layer with a front as-deposited bilayer(front: 30 s i1 + 24 s i2; rear: 81 s i2).

(a) has a *FF* at 79.64%, the J-V curve is well-shaped. As expected the V_{OC} is over 0.71 V since the precursor device is well passivated from Figure 5.5 (a) set4. The deposition of (n)nc-Si:H layer further improves the passivation, and potentially reduce the thickness since the post-HPT effect. Also the front side (i)a-Si:H (~5.6 nm) proves that it is durable to the aggressive plasma condition of the later (n)nc-Si:H deposition, which indicates the appropriate choice of (i)a-Si:H layer.

(b) also has a high V_{OC} at 0.697 mV, this also comes from the good passivation from Figure 5.8 (a). Compared to (a), the *FF* of 77.56% and V_{OC} at 0.697 V are less, which may be explained by the thicker (i)a-Si:H layer and less good passivation

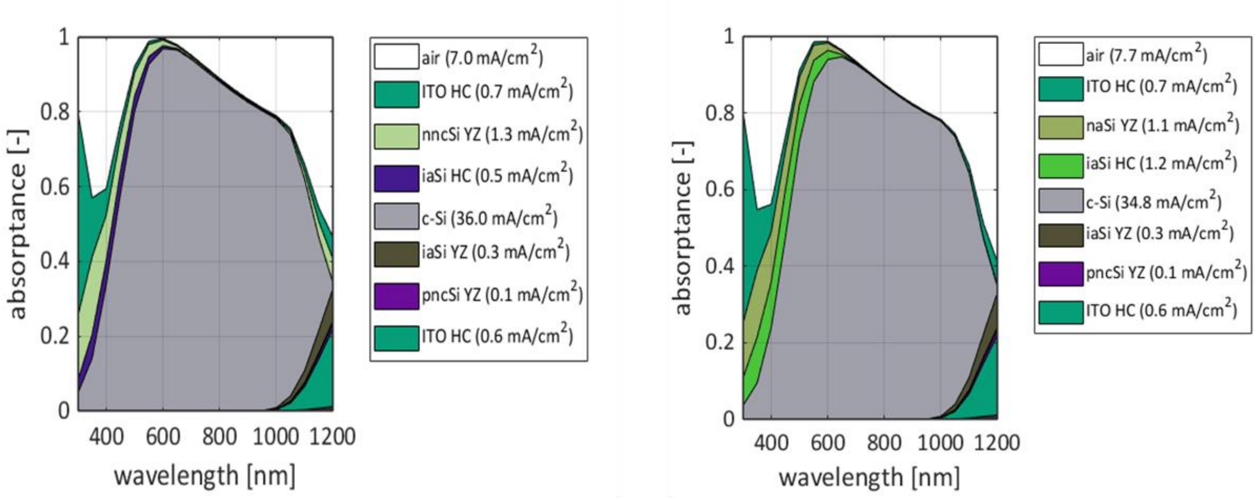

(a) **(b)**

Figure 5.9 GenPro4 [97] *simulation of (a) (n)nc-SI:H champion cell; (b) (n)a-Si champion cell*

Figure 5.9 illustrates the layers' absorptance in solar cells. Compared to (b), the implied photocurrent of (a) is 36 mA/cm^2, the current gain mainly comes from less "air absorptance" and less parasitic absorption of (i)a-Si:H. The less parasitic absorption of cell (a) is because the as-deposited (i)a-Si:H is only 5 nm thick, with the following post-HPT brought by (n)nc-Si:H deposition a thinner (i)a-Si:H is expected, while the thickness of (i)a-Si:H of cell (b) is 9 nm. The GenPro4 model directly shows how the thickness determined parasitic absorption affects the photocurrent. As for the "air absorptance", the white area indicates reflected and transmitted light. In low wavelength range, a doped interlayer with an appropriate refractive index such as nc-SiO$_X$:H can reduce the reflection. And in the long-wavelength range, inserting nanoparticles or dielectric such as MgF$_2$ [98] can increase rear side internal reflectance.

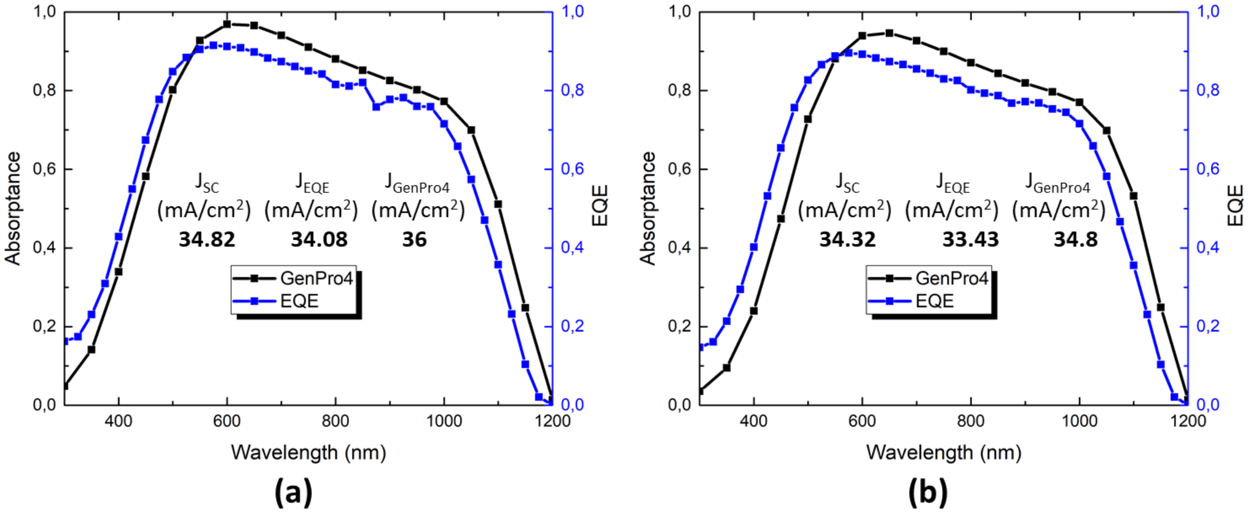

Figure 5.10 The comparison of J_{SC} from J-V measurement, EQE measurement and GenPro4 simulation of (a) (n)nc-SI:H champion cell and (b) (n)a-Si champion cell

Figure 5.10 illustrates the J_{SC} comparison. Since GenPro4 only considers the optical model and ignores the loss in electrical characteristics, $J_{GenPro4}$ is an ideal upper boundary of current. What is interesting is that for both cases J_{EQE} is less than J_{SC} measured from J-V measurement. Theoretically, since there is no metal coverage in EQE measurement which means no shading loss, J_{EQE} should be higher than J_{SC}. A. Desoeudres [95] points out the existing measurement artifacts in EQE measurements for rear-emitter geometry, these phenomenons are explained by that under increased illumination, the emitter properties are better and the charge carrier transport through the a-Si:H layer may be enhanced.

5.6 Summary

In this chapter, the optimized (i)a-Si:H stacks with (n)nc-Si:H (~ 8 nm)/(n)a-Si (~ 6 nm) on the front flat side, rear side is composed by optimized single i2 layer (~ 9 nm) and (p)nc-SiO_X:H (~ 4 nm) + (p)nc-Si:H (~ 16 nm). The highest efficiency of 19.72% is achieved for single-side textured FBC-SHJ solar cell. The highly hydrogen diluted (n)nc-Si:H precursor gas can be regarded as a post-HPT for as-deposited (i)a-Si:H, and the passivation can be improved significantly by the added field effect and also better chemical passivation(by post-HPT). Thinner (i)a-Si:H can improve J_{SC} and *FF* while remains a high V_{OC}, which is not a usual situation in section 4.2. As for EQE measurement, in the infrared range, the EQE is not high enough, which is a challenge in perovskite tandem solar cell.

In the further work the compatibility of (n)nc-SiO_X:H on the front side and the existence of nanoparticles on the rear side is important in improving EQE, especially in the infrared range.

Chapter 6 CONCLUSIONS AND OUTLOOKS

During this project, we start from the passivation (i)a-Si:H optimization, followed by the optimization of front side (n)nc-Si:H/(n)a-Si stack for solar cells fabrication. Based on the awareness of the practical lab work and the existed cell performance, outlooks are proposed for further solar cell efficiency improvement.

6.1 Conclusions

6.1.1 Optimization of (i)a-Si:H

The optimized (i)a-Si:H is essential to have the excellent chemical passivation and surface uniformity. The approach is to adjust the deposition parameters based on their impact on the uniformity and quality of (i)a-Si:H growth. Not only single (i)a-Si:H, but also bilayer structure and HPT are investigated. In this project, a symmetrical 8.8 nm single (i)a-Si:H passivation structure can achieve an effective lifetime at 1.4 ms and implied V_{OC} over 704 mV. A symmetrical 10 nm bilayer (i)a-Si:H passivation structure can achieve an effective lifetime over 8.2 ms and implied V_{OC} over 733 mV.

6.1.2 Optimization of precursor cell

For the front side of the solar cell, the (n)nc-Si:H/(n)a-Si is critical to provide the field-effect passivation, and more importantly, the optimized conditions for (i)a-Si:H and (n)nc-Si:H/(n)a-Si are correlated. This is because the deposition of (n)nc-Si:H/(n)a-Si layer will affect the as-deposited (i)a-Si:H and/or the (i)a-Si:H/(n)c-Si interface. The thickness of (n)nc-Si:H is optimized to offer sufficient passivation protection from TCO sputtering and also less *FF* and J_{SC} loss. As for the rear side, a hydrogen diluted single (i)a-Si:H is used for passivation and a stack of (p)nc-SiO$_X$:H with (p)nc-Si:H is applied.

6.1.3 Fabrication of FBC solar cell

By integrating the optimized layers, the FBC solar cells are eventually fabricated.

In terms of V_{OC}, The highest value is 717 mV. It is found with the 10 nm bilayer structure of (i)a-Si:H. The corresponding SunsV_{OC} is over 730 mV, which indicates a decent passivation quality.

As for J_{SC}, the highest value is 35.1 mA/cm^2. It is realized when we applied a thin (i)a-Si:H (~ 5.6 nm). Meanwhile, the V_{OC} (710 mV) and *FF* (78.53%) are preserved/or improved compared the thicker (i)a-Si:H layer counterpart. This gain in J_{SC} is found to be the main reason for the improved device efficiency.

The champion cell is achieved by applying bilayer (i)a-Si:H (~ 5 nm) and (n)nc-Si:H (~ 8 nm) on the front side. The J_{SC} is 34.82 mA/cm^2, V_{OC} is 711 mV and *FF* is 79.64%. The efficiency is 19.72%.

6.2 Outlooks

6.2.1 (i)a-Si:H optimization

The (i)a-Si:H passivation is thickness dependent and usually the bilayer structure can achieve better passivation but under the thickness around 9 nm. As the conclusion says that the thickness of (i)a-Si:H has a severe impact on J_{SC} gain. The ideal thickness is around 5 nm, which could be the goal for bilayer structure. Actually in AMOR we tried to apply the etching effect of HPT to reduce the total thickness of (i)a-Si:H, but the HPT is not stable in AMOR and then it turns out that we can not preserve passivation under a thinner thickness. In the future, by transferring the recipe from AMOR to AMIGO, the (i)a-Si:H could still be optimized by conducting pressure and HPT. Annealing can also be investigated.

6.2.2 Front side (n)nc-Si:O_X compatibility

An interlayer of (n)nc-SiO_X:H is investigated because of the optimum refractive index (~ 2.6). It is claimed that (n)nc-SiO_X:H can increase the current gain in the infrared range. The deposition condition of (n)nc-SiO_X:H contains a high power (11 W), highly hydrogen diluted gas (DR = 100). This condition is very aggressive that can easily deteriorate the surface passivation. To insert this interlayer on the front side, an investigation of the buffer layer or appropriate thickness of (n)nc-Si:H sublayer can be conducted in the future.

6.2.3 Rear side reflector

The EQE measurement indicates a low utilization of infrared light range, the light is transmitted through the cell. To increase the internal reflectance, a dielectric and nanoparticles can be inserted in between the absorber and rear side metal electrode, such as MgF_2/Ag reflector.

Acknowledgment

I would like to express my great appreciation to the PVMD group that provides me this opportunity to get in touch with this thesis project. Working in the cleaning room and getting involved in PV processing is a very rare experience.

I would like to express my deep gratitude to Dr. Olindo Isabella and Yifeng Zhao, who are my supervisors, for giving me precious suggestions, ideas and inspirations. They spare no effort to facilitate me in lab works, interpretation of results and presentation skills, which is a lifelong benefit for me.

My sincere acknowledgment goes to Dr. Luana Mazarella, Dr. Paul Procel Moya and Dr. Guangtao Yang for helping me to understand the impact of the doped layer on band bending, V_{OC} and FF of a solar cell device. I would like to thank Dr. Rudi Santbergen for the GenPro4 simulation, which has a guiding significance for layer optimization. And I would like to thank Han Can for providing the optimized ITO layer. I also want to thank Dr. Gianluca Limodio for helping me with lab work. Their help enables me to integrate into the PVMD group and have a deep insight into the project.

Special thanks to Martijn Tijssen and Remko Koornneef for their expertise and contribution to maintaining the equipment in good condition.

My special thanks are extended to my friends: Yilong Zhou, Chenrui Zhang and Gilberto Dalla Pozza for the accompany and caring. I would like to thank Tingsen Tu, Zhuohong Xie, Yuyang Zhang, Zi Lin and Ce Deng for your daily caring. Even though we are far apart, I always treasure our invaluable friendship.

Finally, I would like to thank my parents and my family for their selfless dedication, support and love. They are always my solid foundation and the source of motivation.

Hanchen Liu

07th of July, 2020

In Delft, the Netherlands

Bibliography

[1] "Solar Photovoltaic (PV) Market Report 2019: World Solar PV Capacity Estimated to Increase Significantly from 593.9GW in 2019 to 1,582.9GW in 2030." https://www.globenewswire.com/news-release/2019/11/13/1946223/0/en/Solar-Photovoltaic-PV-Market-Report-2019-World-Solar-PV-Capacity-Estimated-to-Increase-Significantly-from-593-9GW-in-2019-to-1-582-9GW-in-2030.html (accessed Jul. 02, 2020).

[2] "New European solar installations to double over next 3 years | Wood Mackenzie." https://www.woodmac.com/press-releases/new-european-solar-installations-to-double-over-next-3-years/ (accessed Jul. 02, 2020).

[3] S. Philipps, F. Ise, and W. Warmuth, "PHOTOVOLTAICS REPORT," 2017. Accessed: Jul. 02, 2020. [Online]. Available: www.ise.fraunhofer.de.

[4] L. K. Wilfried G.J. H.M.van Sark, *Physics and technology of amorphous-crystalline heterojunction silicon solar cells*. 2012.

[5] M. A. Green, "The path to 25% silicon solar cell efficiency: History of silicon cell evolution," *Prog. Photovoltaics Res. Appl.*, vol. 17, no. 3, pp. 183–189, May 2009, doi: 10.1002/pip.892.

[6] T. Mishima, M. Taguchi, H. Sakata, and E. Maruyama, "Development status of high-efficiency HIT solar cells," *Sol. Energy Mater. Sol. Cells*, vol. 95, no. 1, pp. 18–21, 2011, doi: 10.1016/j.solmat.2010.04.030.

[7] T. M. T.Takahama, M.Taguchi, S.Kuroda and S. N. and Y. K. M.Tanaka, S.Tsuda, "No Title," in *11th European Photovoltaic Solar Energy Conference, Montreux*, 1992, pp. 1057–1060.

[8] E. M. Hiroshi Kanno, Daisuke Ide, Yasufumi Tsunomura, Shigeharu Taira, Toshiaki Baba, Yukihiro Yoshimine, Mikio Taguchi, Toshihiro Kinoshita, Hitoshi Sakata, "Over 22% efficient HIT solar cell," in *Proceedings of the 23rd European Photovoltaic Solar Energy Conference*, 2008, pp. 1136–1139.

[9] H. R. Obayes, A. M. AL-Gebori, S. H. Khazaal, A. J. Jarad, G. H. Alwan, and A. A. Al-Amiery, "Hypothetical design of carbon nanotube materials based on [8]circulene," *J. Nanoelectron. Optoelectron.*, vol. 10, no. 5, pp. 711–716, Oct. 2015, doi: 10.1166/jno.2015.1816.

[10] S. Rühle, "Tabulated values of the Shockley-Queisser limit for single junction solar cells," *Sol. Energy*, vol. 130, pp. 139–147, Jun. 2016, doi: 10.1016/j.solener.2016.02.015.

[11] A. Richter, M. Hermle, and S. W. Glunz, "Reassessment of the limiting efficiency for crystalline silicon solar cells," *IEEE J. Photovoltaics*, vol. 3, no. 4, pp. 1184–1191, 2013, doi: 10.1109/JPHOTOV.2013.2270351.

[12] "Technology -." https://qdsolarinc.com/technology/ (accessed Jul. 02, 2020).

[13] "Efficiency Limit of Perovskite/Si Tandem Solar Cells," 2016, doi: 10.1021/acsenergylett.6b00405.

[14] S. Albrecht *et al.*, "Monolithic perovskite/silicon-heterojunction tandem solar cells processed at low temperature," *Energy Environ. Sci.*, vol. 9, no. 1, pp. 81–88, Jan. 2016, doi: 10.1039/c5ee02965a.

[15] L. L. Yan, C. Han, B. Shi, Y. Zhao, and X. D. Zhang, “A review on the crystalline silicon bottom cell for monolithic perovskite/silicon tandem solar cells,” *Mater. Today Nano*, vol. 7, p. 100045, 2019, doi: 10.1016/j.mtnano.2019.100045.

[16] H. Shen *et al.*, “Metal halide perovskite: a game-changer for photovoltaics and solar devices via a tandem design,” *Science and Technology of Advanced Materials*, vol. 19, no. 1. Taylor and Francis Ltd., pp. 53–75, Jan. 01, 2018, doi: 10.1080/14686996.2017.1422365.

[17] Q. Wali, N. K. Elumalai, Y. Iqbal, A. Uddin, and R. Jose, “Tandem perovskite solar cells,” *Renew. Sustain. Energy Rev.*, vol. 84, no. December 2017, pp. 89–110, 2018, doi: 10.1016/j.rser.2018.01.005.

[18] E. Köhnen *et al.*, “Highly efficient monolithic perovskite silicon tandem solar cells: Analyzing the influence of current mismatch on device performance,” *Sustain. Energy Fuels*, vol. 3, no. 8, pp. 1995–2005, 2019, doi: 10.1039/c9se00120d.

[19] G. E. Eperon, M. T. Hörantner, and H. J. Snaith, “Metal halide perovskite tandem and multiple-junction photovoltaics,” *Nat. Rev. Chem.*, vol. 1, no. 12, pp. 1–18, Dec. 2017, doi: 10.1038/s41570-017-0095.

[20] S. Albrecht *et al.*, “Monolithic perovskite/silicon-heterojunction tandem solar cells processed at low temperature,” *Energy Environ. Sci.*, vol. 9, no. 1, pp. 81–88, 2016, doi: 10.1039/c5ee02965a.

[21] Y. Xu *et al.*, “Efficient Hybrid Mesoscopic Solar Cells with Morphology-Controlled CH 3 NH 3 PbI 3-x Cl x Derived from Two-Step Spin Coating Method,” *ACS Publ.*, vol. 7, no. 4, pp. 2242–2248, Feb. 2015, doi: 10.1021/am5057807.

[22] X. Liu *et al.*, “Boosting the efficiency of carbon-based planar CsPbBr3 perovskite solar cells by a modified multistep spin-coating technique and interface engineering,” *Elsevier*, Accessed: Jul. 02, 2020. [Online]. Available: https://www.sciencedirect.com/science/article/pii/S2211285518308668.

[23] C. H. Chiang, Z. L. Tseng, and C. G. Wu, “Planar heterojunction perovskite/PC71BM solar cells with enhanced open-circuit voltage via a (2/1)-step spin-coating process,” *J. Mater. Chem. A*, vol. 2, no. 38, pp. 15897–15903, Oct. 2014, doi: 10.1039/c4ta03674c.

[24] B. Shi *et al.*, “Enhanced light absorption of thin perovskite solar cells using textured substrates,” *Elsevier*, Accessed: Jul. 02, 2020. [Online]. Available: https://www.sciencedirect.com/science/article/pii/S0927024817302076.

[25] C. Haase and H. Stiebig, “Thin-film silicon solar cells with efficient periodic light trapping texture,” *Appl. Phys. Lett.*, vol. 91, no. 6, 2007, doi: 10.1063/1.2768882.

[26] C. Ke, M. Peters, Y. Huang, P. I. Widenborg, and A. G. Aberle, “Theoretical investigation of light trapping in polycrystalline silicon thin-film solar cells,” *Energy Procedia*, vol. 25, pp. 43–49, 2012, doi: 10.1016/j.egypro.2012.07.006.

[27] C. Tsai, G. Anderson, R. T.-J. of non-crystalline solids, and undefined 1991, “Low temperature growth of epitaxial and amorphous silicon in a hydrogen-diluted silane plasma,” *Elsevier*, Accessed: Jul. 02, 2020. [Online]. Available: https://www.sciencedirect.com/science/article/pii/S0022309305802108.

[28] U. K. Das, M. Z. Burrows, M. Lu, S. Bowden, and R. W. Birkmire, “Surface passivation and heterojunction cells on Si (100) and (111) wafers using dc and rf plasma deposited Si:H thin films,” *Appl. Phys. Lett.*, vol. 92, no. 6, pp. 1–4, 2008, doi: 10.1063/1.2857465.

[29] C. Momblona *et al.*, “Efficient vacuum deposited p-i-n and n-i-p perovskite solar cells employing doped charge transport layers,” *Energy Environ. Sci.*, vol. 9, no. 11, pp. 3456–3463, Nov. 2016, doi: 10.1039/c6ee02100j.

[30] J. Temmler, M. Bivour, H. Steinkemper, M. H.-P. 29th E. P. Sol, and undefined 2014, “Boron doped a-SiC: H front layers for silicon heterojunction cells.”

[31] P. P.-P. 36th E. P. S. E. C. Exhib. and undefined 2019, “On the correlation between contact resistivity and high efficiency in (IBC-) SHJ solar cells.”

[32] P. Procel *et al.*, “The role of heterointerfaces and subgap energy states on transport mechanisms in silicon heterojunction solar cells,” *Prog. Photovoltaics Res. Appl.*, no. May, pp. 1–11, 2020, doi: 10.1002/pip.3300.

[33] Y. Nakao and T. Hiyama, “Silicon-based cross-coupling reaction: An environmentally benign version,” *Chem. Soc. Rev.*, vol. 40, no. 10, pp. 4893–4901, Sep. 2011, doi: 10.1039/c1cs15122c.

[34] “File:Silicon-unit-cell-3D-balls.png - Wikimedia Commons.” https://commons.wikimedia.org/wiki/File:Silicon-unit-cell-3D-balls.png (accessed Jul. 02, 2020).

[35] Y. Brahmi, “hydrogenated amorphous and nanocrystalline silicon at the solid / liquid Electrostatic interactions effect on the adsorption of proteins on hydrogenated amorphous and nanocrystalline silicon at the solid / liquid interface PhD Thesis Yamina Brahmi,” no. July, 2018.

[36] A. Goetzberger, J. Knobloch, B. V.-N. York, and undefined 1998, “Crystalline silicon solar cells,” *indico.ictp.it*, Accessed: Jul. 02, 2020. [Online]. Available: http://indico.ictp.it/event/a04253/session/7/contribution/4/material/0/0.pdf.

[37] M. G.- ph and undefined 1982, “Solar cells: operating principles, technology, and system applications,” *ui.adsabs.harvard.edu*, Accessed: Jul. 02, 2020. [Online]. Available: https://ui.adsabs.harvard.edu/abs/1982ph...book.....G/abstract.

[38] H. García *et al.*, “Electrical Characterization of Amorphous Silicon MIS-Based Structures for HIT Solar Cell Applications,” *Nanoscale Res. Lett.*, vol. 11, no. 1, Dec. 2016, doi: 10.1186/s11671-016-1545-z.

[39] S. Das *et al.*, “High-Performance Flexible Perovskite Solar Cells by Using a Combination of Ultrasonic Spray-Coating and Low Thermal Budget Photonic Curing,” 2015, doi: 10.1021/acsphotonics.5b00119.

[40] “Semiconductor Heterojunctions - B. L. Sharma, R. K. Purohit - Google Books.” https://books.google.nl/books?hl=en&lr=&id=PzkXBQAAQBAJ&oi=fnd&pg=PP1&dq=Semiconductor+Heterojunctions&ots=DCOlVfKz0F&sig=GIOwct6cgelR6idt69i-w0NHaRo&redir_esc=y#v=onepage&q=Semiconductor Heterojunctions&f=false (accessed Jul. 02, 2020).

[41] M. Mikolášek, J. Jakabovič, V. Řeháček, L. Harmatha, and R. Andok, “Capacitance analysis of the structures with the a-Si:H(i)/c-Si(p) heterojunction for solar-cell applications,” *J. Electr. Eng.*, vol. 65, no. 4, pp. 254–258, 2014, doi: 10.2478/jee-2014-0039.

[42] F. Jiménez-Molinos, F. Gámiz, A. Palma, P. Cartujo, and J. A. López-Villanueva, “Direct and trap-assisted elastic tunneling through ultrathin gate oxides,” *J. Appl. Phys.*, vol. 91, no. 8, p. 5116, Apr. 2002, doi: 10.1063/1.1461062.

[43] W. Gös, Y. Wimmer, A. El-Sayed, … G. R.-M., and undefined 2018, “Identification of oxide defects in semiconductor devices: A systematic approach linking DFT to rate equations and experimental evidence,” *Elsevier*, Accessed: Jul. 03, 2020. [Online]. Available: https://www.sciencedirect.com/science/article/pii/S0026271417305796.

[44] S. Sze and K. Ng, *Physics of semiconductor devices*. 2006.

[45] M. Ieong, P. Solomon, … S. L.-… D. (Cat. N., and undefined 1998, “Comparison of raised and Schottky source/drain MOSFETs using a novel tunneling contact model,” *ieeexplore.ieee.org*, Accessed: Jul. 03, 2020. [Online]. Available: https://ieeexplore.ieee.org/abstract/document/746461/.

[46] P. Procel, G. Yang, O. Isabella, and M. Zeman, “Theoretical evaluation of contact stack for high efficiency IBC-SHJ solar cells,” *Sol. Energy Mater. Sol. Cells*, vol. 186, no. June, pp. 66–77, 2018, doi: 10.1016/j.solmat.2018.06.021.

[47] S. M., J. Chul, J. Lee, J. Jang, Y.-J. Lee, and J. Yi, “Single- and Multiple-Junction p-i-n Type Amorphous Silicon Solar Cells with p-a-Si1-xCx:H and nc-Si:H Films,” in *Photodiodes - From Fundamentals to Applications*, InTech, 2012.

[48] D. Y. Kim, E. Guijt, R. A. C. M. M. Van Swaaij, and M. Zeman, “Development of a-SiOx:H solar cells with very high Voc×FF product,” *Prog. Photovoltaics Res. Appl.*, vol. 23, no. 6, pp. 671–684, Jun. 2015, doi: 10.1002/pip.2581.

[49] R. Biron, C. Pahud, F. Haug, C. B.-J. of non-crystalline solids, and undefined 2012, “Origin of the Voc enhancement with a p-doped nc-SiOx: H window layer in nip solar cells,” *Elsevier*, Accessed: Jul. 03, 2020. [Online]. Available: https://www.sciencedirect.com/science/article/pii/S0022309312001020.

[50] A. Lambertz, V. Smirnov, T. Merdzhanova, … K. D.-S. E. M., and undefined 2013, “Microcrystalline silicon–oxygen alloys for application in silicon solar cells and modules,” *Elsevier*, Accessed: Jul. 03, 2020. [Online]. Available: https://www.sciencedirect.com/science/article/pii/S0927024813002766.

[51] E. L. Salabaş *et al.*, “Record amorphous silicon single-junction photovoltaic module with 9.1% stabilized conversion efficiency on 1.43 m2,” *Prog. Photovoltaics Res. Appl.*, vol. 24, no. 8, pp. 1068–1074, Aug. 2016, doi: 10.1002/pip.2760.

[52] T. Mueller, W. Duengen, Y. Ma, R. Job, M. Scherff, and W. R. Fahrner, “Investigation of the emitter band gap widening of heterojunction solar cells by use of hydrogenated amorphous carbon silicon alloys,” *J. Appl. Phys.*, vol. 102, no. 7, 2007, doi: 10.1063/1.2785012.

[53] L. Mazzarella *et al.*, “Infrared Light Management Using a Nanocrystalline Silicon Oxide Interlayer in Monolithic Perovskite/Silicon Heterojunction Tandem Solar Cells with Efficiency above 25%,” *Adv. Energy Mater.*, vol. 9, no. 14, pp. 1–9, 2019, doi: 10.1002/aenm.201803241.

[54] S. Olibet, E. Vallat-Sauvain, and C. Ballif, “Model for a-Si:H/c-Si interface recombination based on the amphoteric nature of silicon dangling bonds,” *Phys. Rev. B - Condens. Matter Mater. Phys.*, vol. 76, no. 3, Jul. 2007, doi: 10.1103/PhysRevB.76.035326.

[55] J. Koh, A. S. Ferlauto, P. I. Rovira, C. R. Wronski, and R. W. Collins, “Cite as,” *Appl. Phys. Lett*, vol. 75, no. 15, p. 2286, Oct. 1999, doi: 10.1063/1.124992.

[56] “Substrate dependent growth of microcrystalline silicon,” *ieeexplore.ieee.org*, Accessed: Jul. 02, 2020. [Online]. Available: https://ieeexplore.ieee.org/abstract/document/6925130/.

[57] P. Roca i Cabarrocas, N. Layadi, T. Heitz, B. Drévillon, and I. Solomon, "Substrate selectivity in the formation of microcrystalline silicon: Mechanisms and technological consequences," *Appl. Phys. Lett.*, vol. 66, no. February 1995, p. 3603, 1995, doi: 10.1063/1.113803.

[58] R. Saleh, N. N.-T. S. Films, and undefined 2003, "Raman spectroscopy of B-doped microcrystalline silicon films," *Elsevier*, Accessed: Jul. 02, 2020. [Online]. Available: https://www.sciencedirect.com/science/article/pii/S0040609002012038.

[59] P. Cuony *et al.*, "Silicon filaments in silicon oxide for next-generation photovoltaics," *Adv. Mater.*, vol. 24, no. 9, pp. 1182–1186, Mar. 2012, doi: 10.1002/adma.201104578.

[60] V. M. Vorgelegt, I. Sc, and V. Der Fakultät, "NANOCRYSTALLINE SILICON AND SILICON OXIDE CONTACT LAYERS FOR SILICON HETEROJUNCTION SOLAR CELLS LUANA MAZZARELLA GEB. IN NAPOLI."

[61] P. Babál, *Doped Nanocrystalline Silicon Oxide for use as intermediate reflecting layers in thin-film silicon solar cells*. 2014.

[62] A. H. Simon, *Sputter Processing*. Elsevier Inc., 2018.

[63] "The Future of Screen Printing." https://www.fespa.com/en/news-media/industry/the-future-of-screen-printing (accessed Jul. 02, 2020).

[64] M. Green and M. Keevers, "Optical properties of intrinsic silicon at 300 K," *Prog. Photovoltaics Res. Appl.*, vol. 3, 1995, doi: 10.1002/pip.4670030303.

[65] "Self-consistent optical parameters of intrinsic silicon at 300 K including temperature coefficients," *Sol. Energy Mater. Sol. Cells*, vol. 92, 2008, doi: 10.1016/j.solmat.2008.06.009.

[66] "Optical Properties of Silicon | PVEducation." https://www.pveducation.org/pvcdrom/materials/optical-properties-of-silicon (accessed Jul. 02, 2020).

[67] J. Ge, Z. P. Ling, J. Wong, T. Mueller, and A. G. Aberle, "Optimisation of intrinsic a-Si:H passivation layers in crystalline- amorphous silicon heterojunction solar cells," *Energy Procedia*, vol. 15, no. 2011, pp. 107–117, 2012, doi: 10.1016/j.egypro.2012.02.013.

[68] C. Koch, M. Ito, and M. Schubert, "Low-temperature deposition of amorphous silicon solar cells," *Sol. Energy Mater. Sol. Cells*, vol. 68, no. 2, pp. 227–236, May 2001, doi: 10.1016/S0927-0248(00)00249-X.

[69] Y. Zhao, "Contact Stack Evaluation for SHJ Solar Cells and Process Development of IBC-SHJ Solar Cells," 2018, Accessed: Jul. 02, 2020. [Online]. Available: https://repository.tudelft.nl/islandora/object/uuid:77f483ae-f1da-42c1-8c5a-ae601b140d90.

[70] A. Descoeudres *et al.*, "Improved amorphous/crystalline silicon interface passivation by hydrogen plasma treatment," *Appl. Phys. Lett.*, vol. 99, no. 12, pp. 1–4, 2011, doi: 10.1063/1.3641899.

[71] D. Deligiannis, V. Marioleas, R. Vasudevan, C. C. G. Visser, R. A. C. M. M. Van Swaaij, and M. Zeman, "Understanding the thickness-dependent effective lifetime of crystalline silicon passivated with a thin layer of intrinsic hydrogenated amorphous silicon using a nanometer-accurate wet-etching method," *J. Appl. Phys.*, vol. 119, no. 23, 2016, doi: 10.1063/1.4954069.

[72] H. Hao *et al.*, "Structure, stability and photoelectronic properties of transition films from amorphous to microcrystalline silicon," *Elsevier*, Accessed: Jul. 02, 2020. [Online]. Available: https://www.sciencedirect.com/science/article/pii/S0022024805005312.

[73] J. Hsiao, C. Chen, C. Lin, … D. W.-J. of the, and undefined 2011, “Effect of Hydrogen Dilution on the Intrinsic a-Si:H Film of the Heterojunction Silicon-Based Solar Cell,” *iopscience.iop.org*, vol. 158, no. 9, p. H876, 2011, doi: 10.1149/1.3607981.

[74] R. Gogolin, R. Ferré, M. Turcu, and N. P. Harder, “Silicon heterojunction solar cells: Influence of H 2-dilution on cell performance,” *Sol. Energy Mater. Sol. Cells*, vol. 106, pp. 47–50, 2012, doi: 10.1016/j.solmat.2012.06.001.

[75] V. A. Dao *et al.*, “High-Efficiency Heterojunction with Intrinsic Thin-Layer Solar Cells: A Review,” *Curr. Photovolt. Res.*, vol. 1, no. 12, pp. 73–81, 2013.

[76] E. Bhattacharya and A. H. Mahan, “Microstructure and the light-induced metastability in hydrogenated amorphous silicon,” *Appl. Phys. Lett.*, vol. 52, no. 19, pp. 1587–1589, 1988, doi: 10.1063/1.99089.

[77] U. Kroll, J. Meier, P. Torres, J. Pohl, and A. Shah, “From amorphous to microcrystalline silicon films prepared by hydrogen dilution using the VHF (70 MHz) GD technique,” *J. Non. Cryst. Solids*, vol. 227–230, no. PART 1, pp. 68–72, May 1998, doi: 10.1016/S0022-3093(98)00329-9.

[78] K. Sarakinos, J. Alami, and S. Konstantinidis, “High power pulsed magnetron sputtering: A review on scientific and engineering state of the art,” *Surface and Coatings Technology*, vol. 204, no. 11. Elsevier, pp. 1661–1684, Feb. 25, 2010, doi: 10.1016/j.surfcoat.2009.11.013.

[79] S. Dauwe, J. Schmidt, and R. Hezel, “Very low surface recombination velocities on p- and n-type silicon wafers passivated with hydrogenated amorphous silicon films,” in *Conference Record of the IEEE Photovoltaic Specialists Conference*, 2002, pp. 1246–1249, doi: 10.1109/pvsc.2002.1190834.

[80] M. Mews, T. F. Schulze, N. Mingirulli, and L. Korte, “Amorphous silicon passivation of surfaces promoting epitaxy,” *Energy Procedia*, vol. 38, pp. 855–861, 2013, doi: 10.1016/j.egypro.2013.07.356.

[81] A. Fontcuberta i Morral and P. Roca i Cabarrocas, “Etching and hydrogen diffusion mechanisms during a hydrogen plasma treatment of silicon thin films,” in *Journal of Non-Crystalline Solids*, Apr. 2002, vol. 299–302, no. PART 1, pp. 196–200, doi: 10.1016/S0022-3093(01)01001-8.

[82] S. Sriraman, S. Agarwal, E. S. Aydil, and D. Maroudas, “Mechanism of hydrogen-induced crystallization of amorphous silicon,” *Nature*, vol. 418, no. 6893, pp. 62–65, Jul. 2002, doi: 10.1038/nature00866.

[83] W. Huang *et al.*, “Low temperature PECVD SiNx films applied in OLED packaging,” *Mater. Sci. Eng. B Solid-State Mater. Adv. Technol.*, vol. 98, no. 3, pp. 248–254, Apr. 2003, doi: 10.1016/S0921-5107(03)00045-X.

[84] J. Geissbühler *et al.*, “Amorphous/crystalline silicon interface defects induced by hydrogen plasma treatments,” *Appl. Phys. Lett.*, vol. 102, no. 23, 2013, doi: 10.1063/1.4811253.

[85] H. Sai, P. W. Chen, H. J. Hsu, T. Matsui, S. Nunomura, and K. Matsubara, “Impact of intrinsic amorphous silicon bilayers in silicon heterojunction solar cells,” *J. Appl. Phys.*, vol. 124, no. 10, 2018, doi: 10.1063/1.5045155.

[86] Z. C. Holman *et al.*, “Current losses at the front of silicon heterojunction solar cells,” *IEEE J. Photovoltaics*, vol. 2, no. 1, pp. 7–15, 2012, doi: 10.1109/JPHOTOV.2011.2174967.

[87] R. S. Crandall, E. Iwaniczko, J. V. Li, and M. R. Page, “A comprehensive study of hole collection in heterojunction solar cells,” *J. Appl. Phys.*, vol. 112, no. 9, p. 093713, Nov. 2012, doi:

10.1063/1.4764031.

[88] M. Shinohara *et al.*, “Interaction of hydrogen-terminated Si(100), (110), and (111) surfaces with hydrogen plasma investigated by in situ real-time infrared absorption spectroscopy ARTICLES YOU MAY BE INTERESTED IN,” *J. Vac. Sci. Technol. A*, vol. 21, no. 1, p. 25, Jan. 2003, doi: 10.1116/1.1524146.

[89] J. Haschke, O. Dupré, M. Boccard, C. B.-S. E. M. and Solar, and undefined 2018, “Silicon heterojunction solar cells: Recent technological development and practical aspects-from lab to industry,” *Elsevier*, Accessed: Jul. 02, 2020. [Online]. Available: https://www.sciencedirect.com/science/article/pii/S0927024818303805.

[90] K. Westra, “KOH and TMAH Etching of Bulk Silicon Recipes, Tricks, What is Possible, and What is Impossible,” 2010.

[91] M. S. Jeon, M. Dhamrin, T. Saitoh, and K. Kamisako, “Effect of HF treatment on hydrogenated silicon nitride anti-reflection films quality and optical properties,” in *Conference Record of the 2006 IEEE 4th World Conference on Photovoltaic Energy Conversion, WCPEC-4*, 2006, vol. 2, pp. 1425–1428, doi: 10.1109/WCPEC.2006.279720.

[92] D. Deligiannis *et al.*, “Wet-chemical treatment for improved surface passivation of textured silicon heterojunction solar cells,” *Energy Procedia*, vol. 55, pp. 197–202, 2014, doi: 10.1016/j.egypro.2014.08.117.

[93] G. Limodio *et al.*, “High temperature oxidation pre-treatment of textured c-Si wafers passivated by a-Si:H,” *Mater. Sci. Semicond. Process.*, vol. 97, pp. 67–70, Jul. 2019, doi: 10.1016/j.mssp.2019.03.008.

[94] Y. Zhao *et al.*, “Doped hydrogenated nanocrystalline silicon oxide layers for high-efficiency c-Si heterojunction solar cells,” *Prog. Photovoltaics Res. Appl.*, vol. 28, no. 5, pp. 425–435, May 2020, doi: 10.1002/pip.3256.

[95] A. Descoeudres, Z. C. Holman, L. Barraud, S. Morel, S. De Wolf, and C. Ballif, “>21% Efficient Silicon Heterojunction Solar Cells on N-and P-Type Wafers Compared,” *IEEE J. Photovoltaics*, vol. 3, no. 1, pp. 83–89, 2013, doi: 10.1109/JPHOTOV.2012.2209407.

[96] J. Schmidt, R. Peibst, and R. Brendel, “Surface passivation of crystalline silicon solar cells: Present and future,” *Sol. Energy Mater. Sol. Cells*, vol. 187, no. August, pp. 39–54, 2018, doi: 10.1016/j.solmat.2018.06.047.

[97] R. Santbergen, T. Meguro, … T. S.-I. journal of, and undefined 2017, “GenPro4 optical model for solar cell simulation and its application to multijunction solar cells,” *ieeexplore.ieee.org*, Accessed: Jul. 07, 2020. [Online]. Available: https://ieeexplore.ieee.org/abstract/document/7866819/.

[98] Z. C. Holman, A. Descoeudres, S. De Wolf, and C. Ballif, “Record infrared internal quantum efficiency in silicon heterojunction solar cells with dielectric/metal rear reflectors,” *IEEE J. Photovoltaics*, vol. 3, no. 4, pp. 1243–1249, 2013, doi: 10.1109/JPHOTOV.2013.2276484.